THE ASTRONOMICAL JOURNAL, 164:224 (19pp), 2022 November https://doi.org/10.3847/1538-3881/ac84de

An Analysis of the Eclipsing Binaries HD 71636, V1022 Cassiopeiae, and OT Andromedae

Francis C. Fekel[1], Gregory W. Henry[1], James R. Sowell[2], Ethan R. Partington[2], Joanna M. Wedemeyer[2], and ArjunSinh Nakum[2]

[1] Center of Excellence in Information Systems, Tennessee State University, Nashville, TN 37209, USA; fekel@evans.tsuniv.edu, gregory.w.henry@gmail.com

[2] School of Physics, Georgia Institute of Technology, Atlanta, GA 30332, USA; jim.sowell@physics.gatech.edu

Received 2022 February 28; revised 2022 July 11; accepted 2022 July 22; published 2022 October 28

Abstract

We have obtained high-dispersion spectroscopy and *BV* photometry of two F-type eclipsing binaries, HD 71636 and V1022 Cas, plus the A-type system OT And. Transiting Exoplanet Survey Satellite measurements for each system have also been incorporated. The photometry of HD 71636 enables a more consistent picture of this 5.01331 days, circular-orbit system to emerge. The F2 V primary has a mass of $1.506 \pm 0.002\ M_\odot$ and a radius of $1.583 \pm 0.024\ R_\odot$. The mass of the F5 V secondary is $1.282 \pm 0.002\ M_\odot$, and its radius is $1.314 \pm 0.030\ R_\odot$. Comparison with evolutionary models of the Modules for Experiments in Stellar Astrophysics (MESA) series results in a good fit for a composition of [Fe/H] = 0.12 and an age of 0.9 Gyr. For the F6 V stars of V1022 Cas, our analysis produces a period of 12.15616 days and an eccentricity of 0.312. The two components have nearly equal masses of $1.626 \pm 0.001\ M_\odot$ and $1.607 \pm 0.001\ M_\odot$. The radii of the primary and secondary are $2.570 \pm 0.021\ R_\odot$ and $2.445 \pm 0.022\ R_\odot$, respectively. Comparison with the MESA evolutionary models results in [Fe/H] = 0.08 and an age of 1.87 Gyr. OT And consists of a pair of similar mid-A stars that have an orbital period of 20.85292 days and an eccentricity of 0.215. The primary has a mass of $2.253 \pm 0.014\ M_\odot$ and a radius of $3.167 \pm 0.013\ R_\odot$. The corresponding parameters for the secondary are $2.147 \pm 0.011\ M_\odot$ and $2.649 \pm 0.015\ R_\odot$, respectively. The MESA series models produce a best fit for this system with [Fe/H] = 0.10 and an age of 0.675 Gyr. The total apsidal motion in both eccentric systems is less than $1\overset{\circ}{.}5$ century^{-1}.

Unified Astronomy Thesaurus concepts: Spectroscopic binary stars (1557); Fundamental parameters of stars (555); Eclipsing binary stars (444); Detached binary stars (375)

Supporting material: machine-readable tables

1. Introduction

In this paper we report on extensive spectroscopy and photometry that enable us to redetermine the basic properties of two F-type eclipsing binaries, HD 71636 = BD+37 1868 = HIP 41691 = TYC 2489-1972-1 = Gaia EDR3 904854746325664000 ($\alpha = 08^h\ 29^m\ 56\overset{s}{.}312$, $\delta = +37°\ 04'\ 15\overset{''}{.}48$ [2000]), and V1022 Cas = HR 9059 = HD 224355 = BD +54 3076 = HIP 118077 = TYC 4005-1055-1 = Gaia EDR3 1994714276926012 416 ($\alpha = 23^h\ 57^m\ 08\overset{s}{.}472$, $\delta = +55°\ 42'\ 20\overset{''}{.}54$ [2000]), and we determine for the first time the basic properties of the mid-A star eclipsing binary HD 219989 = BD+40 5049 = HIP 115200 = TYC 3238-1651-1 = Gaia EDR3 1924490187240994816 ($\alpha = 23^h\ 20^m\ 01\overset{s}{.}217$, $\delta = +41°\ 45'\ 17\overset{''}{.}46$ [2000]). Henry et al. (2006) initially determined the basic parameters of HD 71636 from a solution of their spectroscopy and photometry, and Clausen et al. (2010) later reanalyzed their data. For V1022 Cas, Lester et al. (2019) calculated the masses of the components by simultaneously determining both the visual and spectroscopic orbits of the system. Recently, Southworth (2021) analyzed the Transiting Exoplanet Survey Satellite (TESS; Ricker et al. 2015) light curves and previous radial velocities to obtain improved basic parameters. The light curve of the eclipsing binary OT And has not previously been analyzed to determine the components' basic properties.

1.1. HD 71636

In a radial-velocity survey of F stars, Nordström et al. (2004) detected the velocity variability of HD 71636. Shortly thereafter, Henry et al. (2005) discovered it to be an eclipsing binary with an orbital period of 5.013 days. Henry et al. (2006) studied HD 71636 in detail, obtaining a simultaneous solution of the eclipse light curves and radial-velocity observations that resulted in an orbital period of 5.01329 days and a circular orbit. Unfortunately, comparison of the components' basic properties with theoretical evolutionary tracks did not provide full consistency. Clausen et al. (2010) compared a group of well-studied eclipsing binaries, which had components in the 1.15–1.70 $M_\odot$ range, with theoretical evolutionary models. They opined that their sample of binaries in this mass range plus others to be observed in the future could be used to improve core overshoot treatment and other ingredients of theoretical models. HD 71636 was initially included in their sample, but, like Henry et al. (2006), they were unable to obtain a consistent age for its two components from theoretical models. Clausen et al. (2010) suggested that the radii values might be the problem because the secondary eclipse was poorly covered. They recommended that it be reobserved to improve the masses and radii of its components. As a result, we have obtained additional Johnson *BV* photometry, especially of the secondary eclipse, plus supplementary radial velocities. The orbital elements and absolute dimensions have been computed with the use of TESS photometry, our new data, and that of Henry et al. (2006).

1.2. V1022 Cas = HD 224355

HD 224355 has been known as a double-lined binary for over 100 yr (Plaskett et al. 1920). The system has a period of 12.156 days and an eccentric orbit (Harper 1923). Its early history was extensively discussed by Fekel et al. (2010). Otero (2006) examined its Hipparcos photometry (ESA 1997) and found this mid-F system to be an eclipsing binary, although the secondary eclipse was unobserved. As a result of that discovery, Kazarovets et al. (2008) assigned it the variable star name V1022 Cas. With an extensive number of new radial velocities, Fekel et al. (2010) determined an improved spectroscopic orbit, provided an updated ephemeris for the eclipses, and noted that the system could be resolved interferometrically. Lester et al. (2019) used the CHARA array to obtain nine interferometric observations and acquired new radial velocities on 16 nights. Their combined visual-spectroscopic orbit, which included the radial velocities from Fekel et al. (2010), resulted in the masses of the components, and additional analyses produced the radii and other basic parameters of the system. Very recently, Southworth (2021) determined the masses, radii, and other basic properties of the components of V1022 Cas utilizing TESS photometry, the velocities of Fekel et al. (2010), and the temperatures derived by Lester et al. (2019).

We have obtained new differential Johnson *BV* photometry that covers both eclipses plus additional radial-velocity measurements. We utilize our new data and the radial velocities of Fekel et al. (2010), along with TESS measurements, to determine the basic properties of the system. Our new analysis provides a useful opportunity to compare results from our ground-based eclipse light-curve and radial-velocity orbit solutions with the TESS photometry solution (Southworth 2021) as well as with the combined visual and spectroscopic orbital solution, which includes a spectral energy distribution (SED) analysis (Lester et al. 2019).

1.3. OT And = HD 219989

Tremko & Bakos (1978) used HD 219989 as a comparison star for their photometric observations of the short-period eclipsing binary AN And, but found no evidence that HD 219989 is a variable star. Crawford (1975a) also used HD 219989 as a comparison star for his observations of AN And and detected the variability of HD 219989. As a result, he began to observe the star separately and detected its eclipses. Hall (1983) put out a call for additional observations of this system. A network of mostly amateur astronomers responded with new observations from which Crawford et al. (1984) were able to determine that this eclipsing binary has a period of 20.8529 days and an eccentric orbit. They also acquired a spectrum that showed double lines and estimated the spectral types of both components to be A3 V. This led Kholopov et al. (1987) to give it the variable star name OT And. Over the succeeding decades, Husar (2005) obtained timings of a primary and a secondary eclipse. We acquired new differential *BV* photometric and radial-velocity measurements. Our new data and TESS photometry are used to obtain eclipsing binary and orbital solutions that result in masses, radii, and other basic properties of the binary A-type components.

2. Spectroscopic Observations and Reductions

2.1. HD 71636

To add to the 14 radial velocities obtained by Henry et al. (2006), we have acquired 56 double-lined spectra of HD 71636 from 2015 October to 2019 March at Fairborn Observatory in southeast Arizona (Eaton & Williamson 2004). We obtained the spectra with the Tennessee State University 2 m Automatic Spectroscopic Telescope (AST) and a fiber-fed echelle spectrograph (Eaton & Williamson 2007). The detector was a Fairchild 486 CCD that has a 4×4 K array of 15 μm pixels (Fekel et al. 2013). The size of the array results in a wavelength coverage that ranges from 3800 to 8260 Å. The spectra have a resolution of 0.24 Å, corresponding to a resolving power of 25,000 at 6000 Å. The best spectra have signal-to-noise ratios (S/Ns) of about 70.

Fekel et al. (2009) have provided a general description of the typical velocity reduction. Specifically, for HD 71636 we used a solar line list that contains 168 mostly neutral Fe lines in the spectral region 4920–7100 Å. Each line was fitted with a rotational broadening function (Sandberg Lacy & Fekel 2011; Fekel & Griffin 2011). Unpublished velocities that were obtained with the AST, its echelle spectrograph, and the Fairchild 486 CCD for several IAU solar-type velocity standard stars show that our velocities with this CCD have a -0.6 km s^{-1} shift relative to the results of Scarfe (2010), so we have added 0.6 km s^{-1} to all our velocities. The velocities of Henry et al. (2006) and our new spectroscopic observations are listed in Table 1.

2.2. V1022 Cas

To supplement the 110 observations previously obtained by Fekel et al. (2010), we acquired 79 additional double-lined spectroscopic observations of V1022 Cas, from 2010 June to 2020 January, at Fairborn Observatory (Eaton & Williamson 2004). As with HD 71636, we used the Tennessee State University 2 m AST and its associated fiber-fed echelle spectrograph (Eaton & Williamson 2007). While the first of these new observations was obtained with our old SITe CCD, described in Fekel et al. (2010), the rest of our new spectra were collected with the Fairchild CCD noted above. The spectra of V1022 Cas also have a resolution of 0.24 Å, corresponding to a resolving power of 25,000 at 6000 Å. The best spectra have a S/N of about 125.

As we did for HD 71636, we used our solar line list, but, in the case of V1022 Cas we fit the individual lines with a Gaussian function to be consistent with the velocity measurements made by Fekel et al. (2010). We have added 0.3 km s^{-1} to the lone velocity that was obtained with our old CCD system and 0.6 km s^{-1} to the rest of our velocities. The spectroscopic observations of Fekel et al. (2010) and our new observations are listed in Table 2.

2.3. OT And

From 2004 September to 2021 May, we acquired 57 useful observations of OT And with our Tennessee State University 2 m AST and its associated fiber-fed echelle spectrograph (Eaton & Williamson 2007). The detector for the first three observations was our original SITe CCD, while the Fairchild CCD (Fekel et al. 2013) was used to collect the rest of our spectra. The spectra with the SITe CCD have a resolution of 0.17 Å,

Table 1
Radial-velocity Observations of HD 71636

Hel. Julian Date HJD−2400000	Phase[a]	RV_1 (km s^{-1})	$(O-C)_1$ (km s^{-1})	Wt_1	RV_2 (km s^{-1})	$(O-C)_2$ (km s^{-1})	Wt_2	Observatory[b]
52705.7320	0.839	44.5	−0.6	0.3	−48.0	−0.7	0.3	KPNO
52706.7880	0.049	79.3	0.1	0.3	−88.0	−0.8	0.3	KPNO
52708.7510	0.441	−72.6	−0.2	0.3	90.5	0.2	0.3	KPNO
52755.6730	0.800	27.8	0.2	0.3	−27.0	−0.2	0.3	KPNO
52756.6550	0.996	83.3	0.3	0.3	−91.6	0.0	0.3	KPNO
52757.6740	0.199	28.7	1.0	0.3	−26.9	0.0	0.3	KPNO
52758.6820	0.401	−62.0	0.7	0.3	78.9	−0.1	0.3	KPNO
52759.7070	0.605	−60.5	0.5	0.3	77.8	0.8	0.3	KPNO
52760.6520	0.794	24.9	0.6	0.3	−23.5	−0.6	0.3	KPNO
52904.0110	0.389	−58.7	0.5	0.3	74.8	0.0	0.3	KPNO
52905.0010	0.587	−66.4	−0.1	0.3	82.5	−0.7	0.3	KPNO
52941.9790	0.963	80.1	−0.7	0.3	−89.4	−0.3	0.3	KPNO
53277.0040	0.790	22.7	0.3	0.3	−20.6	0.1	0.3	KPNO
53278.0100	0.990	82.7	−0.1	0.3	−91.5	0.0	0.3	KPNO
57297.0012	0.654	−42.8	0.4	1.0	55.9	−0.2	1.0	Fair
57322.8822	0.816	35.5	0.4	1.0	−35.6	0.0	1.0	Fair
57346.8911	0.605	−60.6	0.3	1.0	77.0	0.1	1.0	Fair
57374.9053	0.193	31.2	0.6	1.0	−29.9	0.4	1.0	Fair
57399.9243	0.184	35.4	0.4	1.0	−35.5	0.0	1.0	Fair
57415.8119	0.353	−45.8	0.1	1.0	59.1	−0.2	1.0	Fair
57429.9890	0.181	36.5	0.1	1.0	−37.3	−0.1	1.0	Fair
57430.6070	0.304	−24.1	0.1	1.0	33.8	−0.1	1.0	Fair
57431.7450	0.531	−76.2	0.2	1.0	95.0	0.0	1.0	Fair
57433.8340	0.948	78.7	0.0	1.0	−86.8	−0.1	1.0	Fair
57434.6094	0.102	66.9	0.0	1.0	−73.4	−0.5	1.0	Fair
57435.6138	0.303	−23.6	0.0	1.0	33.6	0.4	1.0	Fair
57440.7528	0.328	−35.2	0.0	1.0	46.2	−0.6	1.0	Fair
57443.7424	0.924	74.1	0.1	1.0	−81.2	−0.1	1.0	Fair
57450.8129	0.334	−38.2	0.0	1.0	49.8	−0.4	1.0	Fair
57470.7319	0.308	−26.4	−0.4	1.0	35.9	0.0	1.0	Fair
57492.7949	0.709	−18.9	−0.7	1.0	27.0	0.2	1.0	Fair
57501.7208	0.489	−77.7	0.0	1.0	95.9	−0.6	1.0	Fair
57502.6519	0.675	−34.1	0.0	1.0	45.3	−0.2	1.0	Fair
57503.6482	0.873	59.0	0.2	1.0	−63.6	−0.2	1.0	Fair
57504.6487	0.073	74.6	0.0	1.0	−82.1	−0.2	1.0	Fair
57511.6577	0.471	−76.2	0.4	1.0	94.9	−0.3	1.0	Fair
57513.6647	0.871	58.5	0.3	1.0	−62.8	−0.2	1.0	Fair
57514.6552	0.069	75.4	−0.1	1.0	−83.0	−0.1	1.0	Fair
57516.6658	0.470	−76.3	0.2	1.0	94.4	−0.7	1.0	Fair
57517.6667	0.670	−36.3	0.0	1.0	47.9	−0.2	1.0	Fair
57518.6570	0.867	56.7	0.1	1.0	−60.9	−0.2	1.0	Fair
57519.6569	0.067	76.2	0.1	1.0	−83.4	0.1	1.0	Fair
57521.6792	0.470	−76.0	0.5	1.0	94.6	−0.5	1.0	Fair
57524.6593	0.065	76.1	−0.4	1.0	−84.6	−0.6	1.0	Fair
57534.6604	0.059	77.5	0.1	1.0	−85.4	−0.2	1.0	Fair
57536.6818	0.463	−75.6	0.1	1.0	93.8	−0.4	1.0	Fair
57539.6787	0.060	77.3	0.0	1.0	−85.2	−0.3	1.0	Fair
57648.9601	0.859	53.7	0.4	1.0	−56.7	0.2	1.0	Fair
57676.9727	0.446	−73.0	0.3	1.0	91.2	−0.2	1.0	Fair
57702.8393	0.606	−60.5	0.3	1.0	77.2	0.5	1.0	Fair
57728.0509	0.635	−50.5	0.3	1.0	65.1	0.1	1.0	Fair
57760.8192	0.171	40.8	0.0	1.0	−42.0	0.3	1.0	Fair
57779.8984	0.977	82.4	0.2	1.0	−90.7	0.0	1.0	Fair
57814.8244	0.943	78.2	0.3	1.0	−86.0	−0.2	1.0	Fair
57841.8527	0.335	−38.0	0.3	1.0	50.6	0.3	1.0	Fair
57866.6477	0.281	−13.1	−0.3	1.0	20.1	−0.4	1.0	Fair
57892.6590	0.469	−76.2	0.2	1.0	94.9	0.0	1.0	Fair
57895.7142	0.078	73.7	0.3	1.0	−80.5	0.0	1.0	Fair
58014.9409	0.860	54.2	0.3	1.0	−58.2	−0.5	1.0	Fair
58038.8704	0.634	−51.0	0.1	1.0	65.2	−0.3	1.0	Fair
58075.9289	0.026	82.0	0.1	1.0	−89.9	0.5	1.0	Fair
58110.9486	0.011	82.9	0.1	1.0	−91.6	−0.1	1.0	Fair
58141.7282	0.151	49.9	0.3	1.0	−52.9	−0.3	1.0	Fair

Table 1
(Continued)

Hel. Julian Date HJD−2400000	Phase[a]	RV_1 (km s^{-1})	$(O-C)_1$ (km s^{-1})	Wt_1	RV_2 (km s^{-1})	$(O-C)_2$ (km s^{-1})	Wt_2	Observatory[b]
58160.7336	0.942	77.5	−0.2	1.0	−86.1	−0.7	1.0	Fair
58197.8161	0.338	−40.1	−0.3	1.0	51.8	−0.4	1.0	Fair
58236.7217	0.099	67.7	−0.3	1.0	−74.6	−0.5	1.0	Fair
58430.8133	0.814	34.6	0.6	1.0	−33.8	0.6	1.0	Fair
58475.9247	0.812	33.6	0.4	1.0	−33.0	0.4	1.0	Fair
58526.8889	0.978	82.3	0.0	1.0	−90.4	0.4	1.0	Fair
58571.7465	0.926	74.9	0.5	1.0	−81.9	−0.2	1.0	Fair

Notes.
[a] Phases have been computed with the Period (P) and Epoch (T_0) values of our new spectroscopic solution (Table 4).
[b] KPNO = Kitt Peak National Observatory; Fair = Fairborn Observatory.

(This table is available in its entirety in machine-readable form.)

corresponding to a resolving power of 35,000. The spectra with the new Fairchild CCD have a resolution of 0.4 Å and a resolving power of 15,000. The best spectra have a S/N of 150.

In the case of OT And, we used our A star line list, which consists of 38 mostly singly ionized metal lines within the wavelength range 4920–7100 Å. Each line was fitted with a rotational broadening function (Sandberg Lacy & Fekel 2011; Fekel & Griffin 2011). The lines of both components are significantly broadened, $v \sin i = 58 \pm 2$ km s^{-1} and 59 ± 2 km s^{-1} for the primary and secondary, respectively, and are relatively weak compared to the two solar-type stars discussed above. Thus, we only measured velocities at phases close to the quadratures, when the lines of the components are fully separated or just slightly blended. We added 0.3 km s^{-1} to the velocities obtained with the SITe CCD and 0.6 km s^{-1} to the rest. Our spectroscopic observations are listed in Table 3.

3. Spectroscopic Orbit

3.1. HD 71636

As mentioned earlier, Henry et al. (2006) determined a circular orbit with a period of 5.01329 days for HD 71636. Because of that result, we initially obtained circular-orbit solutions with the computer program SB1C (D. Barlow 1998, private communication) of the four data sets, which are the velocities for the Kitt Peak National Observatory (KPNO) primary, KPNO secondary, Fairborn primary, and Fairborn secondary. That program iterates sine/cosine fits by differential corrections to obtain a least-squares fit. The variances of those four solutions are inversely proportional to the weights that we have adopted for those sets of velocities. As a result, we assigned weights of 0.3 to the KPNO primary and secondary velocities and weights of 1.0 to the Fairborn primary and secondary velocities. Using the appropriately weighted velocities, 70 for each component, we then determined a circular-orbit solution with the computer program SB2C, which is a slightly modified version of SB1C. Because the orbit is circular, the element T, the time of periastron passage, is indeterminate. So, as recommended by Batten et al. (1989), T_0, a time of maximum radial velocity of the primary, which occurs 0.25 in phase before primary eclipse, was determined instead. In Table 4 the new orbital elements are compared with those of Henry et al. (2006). The two sets are very similar although our new elements have significantly improved uncertainties. In Figure 1 the radial velocities are compared with the computed velocity curves while the residuals to the fits, the observed minus computed velocities, are plotted in Figure 2.

3.2. V1022 Cas

Adopting the orbital elements of Fekel et al. (2010) as starting values, we obtained six separate orbital solutions with the computer program SB1 (Barker et al. 1967) for the velocities of the primary and secondary that were obtained at the KPNO, McDonald, and Fairborn observatories. We did not include the radial velocities measured by Lester et al. (2019) because they are significantly less numerous, less precise, and within the date range of our velocities. The SB1 program computes the elements by differential corrections. The lines of the two components are reasonably similar in depth and width, and so from each observatory the velocity weights for the two stars are similar. Comparison of the variances resulted in weights of 1.0 for the McDonald velocities, 0.5 for the Fairborn velocities, and 0.3 for the KPNO velocities. We obtained final spectroscopic orbital elements by simultaneously fitting the weighted velocities of both components using the orbit program SB2, a slightly modified version of SB1. Those elements and related quantities are listed in Table 5. The spectroscopic elements are very similar to those of Fekel et al. (2010) but have smaller uncertainties. The resulting minimum masses of the components are nearly identical. Figure 3 compares the radial velocities with the computed velocity curves, and the residuals to the fits are plotted in Figure 4.

3.3. OT And

From the photometric results of Crawford et al. (1984), we adopted a period of 20.8529 days and determined preliminary orbital elements for the primary with the program BISP (Wolfe et al. 1967), which uses a slightly modified version of the Wilsing–Russell method. We then obtained individual solutions of the primary and secondary with SB1 (Barker et al. 1967).

Comparison of the variances of the two solutions resulted in assigned weights of 1.0 for the primary velocities and 0.5 for the secondary velocities. We acquired final spectroscopic orbital elements by simultaneously fitting the weighted velocities of both components using the orbit program SB2, a slightly modified version of SB1. Those elements and related quantities are listed in Table 6. Figure 5 compares the radial velocities with the computed velocity curves, while the residuals to the fits are plotted in Figure 6.

Table 2
Radial-velocity Observations of V1022 Cas

Hel. Julian Date HJD−2400000	Phase[a]	RV_1 (km s^{-1})	$(O-C)_1$ (km s^{-1})	Wt_1	RV_2 (km s^{-1})	$(O-C)_2$ (km s^{-1})	Wt_2	Observatory[b]
53170.988	0.842	67.3	−0.4	0.3	−44.8	0.0	0.3	KPNO
53172.979	0.005	85.6	−0.3	0.3	−63.6	−0.4	0.3	KPNO
53259.883	0.154	−10.9	0.1	1.0	34.8	0.0	1.0	McD
53261.854	0.316	−40.8	0.1	1.0	65.0	0.0	1.0	McD
53273.787	0.298	−40.2	0.0	0.3	64.1	−0.3	0.3	KPNO
53275.768	0.461	−32.9	0.6	0.3	57.6	0.0	0.3	KPNO
53277.852	0.632	−3.3	0.4	0.3	27.2	−0.2	0.3	KPNO
53278.011	0.646	−0.4	0.1	0.5	24.2	0.0	0.5	Fair
53287.916	0.460	−33.6	0.0	0.5	57.8	0.1	0.5	Fair
53313.791	0.589	−13.3	0.0	0.5	37.3	0.1	0.5	Fair
53322.937	0.341	−41.3	−0.2	0.5	65.3	0.1	0.5	Fair
53341.922	0.903	92.5	0.2	0.5	−69.7	0.0	0.5	Fair
53342.687	0.966	100.3	0.3	1.0	−77.2	0.3	1.0	McD
53354.817	0.964	100.2	−0.1	0.5	−77.8	0.0	0.5	Fair
53360.730	0.450	−34.8	−0.1	0.5	58.4	−0.4	0.5	Fair
53432.594	0.362	−40.9	−0.2	0.5	64.6	−0.3	0.5	Fair
53437.647	0.778	41.3	0.0	0.5	−18.5	−0.4	0.5	Fair
53464.955	0.024	74.4	0.3	0.5	−51.7	−0.4	0.5	Fair
53478.913	0.172	−17.9	0.0	0.5	41.6	−0.2	0.5	Fair
53491.901	0.241	−34.7	−0.1	0.5	58.6	−0.1	0.5	Fair
53504.845	0.306	−40.5	0.0	0.5	64.4	−0.3	0.5	Fair
53528.796	0.276	−38.7	0.0	0.5	62.8	−0.1	0.5	Fair
53531.958	0.536	−23.3	−0.2	0.3	46.4	−0.7	0.3	KPNO
53534.969	0.784	43.3	−0.3	0.3	−20.6	−0.1	0.3	KPNO
53535.983	0.867	78.3	−0.3	0.3	−56.0	−0.2	0.3	KPNO

Notes.
[a] Phases have been computed with the Period (*P*) and Epoch (*T*) values of our new spectroscopic solution (Table 5).
[b] KPNO = Kitt Peak National Observatory; McD = McDonald Observatory; Fair = Fairborn Observatory.

(This table is available in its entirety in machine-readable form.)

4. Photometric Observations and Reductions

Our photometric observations of HD 71636, V1022 Cas, and OT And were acquired in the Johnson *V* and *B* passbands with the T3 0.40 m automatic photoelectric telescope (APT) at Fairborn Observatory in southeast Arizona. Observations of all three targets were made differentially with respect to nearby comparison and check stars in the group sequence described by Henry et al. (2006) that was used for our earlier observations of HD 71636. All differential magnitudes were corrected for extinction and transformed to the standard Johnson *UBV* system with coefficients determined from nightly observations of standard stars. Additional information on the operation of the T3 APT and the analysis of the data can be found in Henry (1995a), Henry (1995b), and Eaton et al. (2003).

Southworth (2022) has provided a brief overview of TESS, its program of observation, and the resulting photometric observations, which can be used for eclipsing binary light-curve analysis. The TESS photometric observations for our three systems were downloaded from the Mikulski Archive for Space Telescopes.[3] We converted the simple aperture photometry fluxes to magnitudes, and subtracted these from 14 mag for HD 71636 and OT And, whereas 16 mag was used for the V1022 Cas calculation. Often there are tens of thousands of data points in the fully observed TESS light curves. Because all three of our systems have spherically shaped stars and no star spots, the out-of-eclipse portions of the light curves contain little information on the stellar properties. Consequently, while we incorporated all of the primary and secondary eclipse measurements, we only utilized a handful of out-of-eclipse observations in the TESS analyses.

4.1. HD 71636

Our new observations of HD 71636 were obtained between 2015 September and 2017 April, primarily to improve coverage of the secondary eclipse. Together with our older observations in Henry et al. (2006) that were collected between 2002 September and 2003 May, we have a total of 717 group mean differential magnitudes in *V* and 729 in *B*. All of the old and new differential magnitudes are computed against the comparison star HD 72184 and are given in Table 7 along with the heliocentric Julian dates and the orbital phases computed with the BV+TESS photometric ephemeris given in Table 12 of Section 5. The TESS photometry covers most of the eclipses from HJD 2,459,580 through HJD 2,459,606, which included five primary eclipses and four secondaries. The number of measurements used was 1983.

4.2. V1022 Cas

Between 2009 December and 2018 June we acquired 1421 photometric observations in *V* and 1422 in *B* of V1022 Cas. For most nights, a single observation consists of the group mean of three differential measurements of V1022 Cas minus the comparison star (HD 224784). On nights when our orbital ephemeris predicted conjunctions of the two stars, we modified

[3] https://mast.stsci.edu/portal/Mashup/Clients/Mast/Portal.html

Table 3
Radial-velocity Observations of OT And

Hel. Julian Date HJD−2400000	Phase[a]	RV_1 (km s^{-1})	$(O-C)_1$ (km s^{-1})	Wt_1	RV_2 (km s^{-1})	$(O-C)_2$ (km s^{-1})	Wt_2
53276.8877	0.814	−70.7	−1.6	1.0	65.2	2.6	0.5
53319.8418	0.874	−69.6	1.0	1.0	62.9	−1.3	0.5
53341.7884	0.927	−62.9	−3.1	1.0	52.4	−0.4	0.5
55489.6684	0.927	−59.8	−0.2	1.0	51.5	−1.1	0.5
55516.8254	0.229	58.2	3.2	1.0	−67.9	−0.2	0.5
55528.7853	0.803	−66.9	0.7	1.0	59.7	−1.4	0.5
55675.9677	0.861	−71.1	0.3	1.0	64.0	−0.9	0.5
55842.6285	0.853	−70.5	1.0	1.0	62.9	−2.2	0.5
55869.7734	0.155	49.3	−0.9	1.0	−62.7	−0.1	0.5
55893.5669	0.296	51.3	2.2	1.0	−58.4	3.0	0.5
55953.6150	0.175	54.4	1.2	1.0	−59.8	5.9	0.5
56194.6395	0.734	−52.1	2.2	1.0	52.6	5.6	0.5
56195.6457	0.782	−65.3	−1.0	1.0	58.1	0.5	0.5
56196.6048	0.828	−70.7	−0.3	1.0	63.9	−0.1	0.5
56197.6882	0.880	−70.1	0.0	1.0	62.8	−0.8	0.5
56216.5915	0.786	−66.6	−1.5	1.0	54.8	−3.6	0.5
56218.5914	0.882	−72.8	−3.0	1.0	60.2	−3.1	0.5
56219.5896	0.930	−56.9	1.7	1.0	53.3	1.8	0.5
56224.5979	0.170	52.7	0.1	1.0	−65.7	−0.6	0.5
56225.5861	0.218	54.1	−1.2	1.0	−65.2	2.7	0.5
56226.5851	0.266	52.7	0.0	1.0	−61.4	3.8	0.5
56237.5860	0.793	−67.5	−1.3	1.0	60.1	0.6	0.5
56246.5815	0.225	57.5	2.3	1.0	−67.0	0.8	0.5
56266.5669	0.183	53.3	−0.6	1.0	−68.1	−1.6	0.5
56267.5668	0.231	54.0	−1.0	1.0	−64.8	2.8	0.5
56268.5664	0.279	50.9	−0.4	1.0	−65.5	−1.8	0.5
56279.6092	0.808	−67.4	1.0	1.0	63.2	1.4	0.5
56433.9227	0.208	56.4	1.2	1.0	−67.3	0.6	0.5
56468.8291	0.882	−67.1	2.7	1.0	62.1	−1.2	0.5
56557.7792	0.148	45.6	−3.2	1.0	−64.2	−3.1	0.5
56579.6512	0.197	55.2	0.4	1.0	−66.0	1.5	0.5
56601.5795	0.248	51.5	−2.6	1.0	−66.6	0.1	0.5
56613.5846	0.824	−68.3	1.8	1.0	61.3	−2.3	0.5
56614.5732	0.871	−70.3	0.5	1.0	62.9	−1.5	0.5
56622.5836	0.256	53.8	0.2	1.0	−68.3	−2.2	0.5
56685.6200	0.278	47.9	−3.4	1.0	−62.9	0.9	0.5
56787.9071	0.184	53.1	−0.9	1.0	−66.8	−0.2	0.5
56823.8387	0.907	−64.1	1.4	1.0	58.1	−0.8	0.5
57280.7031	0.815	−71.5	−2.3	1.0	63.4	0.7	0.5
57324.6761	0.924	−60.5	0.2	1.0	55.4	1.7	0.5
57551.8547	0.818	−69.0	0.5	1.0	62.1	−0.9	0.5
57675.7095	0.758	−59.7	−0.1	1.0	53.7	1.1	0.5
57705.6874	0.195	55.3	0.5	1.0	−70.0	−2.6	0.5
57727.7651	0.254	53.5	−0.2	1.0	−67.9	−1.7	0.5
57863.9856	0.786	−64.3	0.8	1.0	58.2	−0.2	0.5
58017.8376	0.164	53.2	1.5	1.0	−61.7	2.5	0.5
58040.6757	0.259	50.9	−2.3	1.0	−65.3	0.5	0.5
58095.5684	0.892	−69.3	−0.8	1.0	64.7	2.8	0.5
58762.6074	0.879	−68.4	1.7	1.0	67.9	4.2	0.5
58769.5960	0.214	55.3	0.0	1.0	−67.1	0.8	0.5
58782.5872	0.837	−72.4	−1.4	1.0	65.2	0.6	0.5
58783.5866	0.885	−70.0	−0.6	1.0	65.4	2.5	0.5
58789.5832	0.173	52.1	−0.8	1.0	−69.4	−4.0	0.5
58790.5825	0.221	57.6	2.4	1.0	−68.2	−0.3	0.5
58791.5816	0.269	52.2	−0.2	1.0	−66.2	−1.3	0.5
59138.8182	0.920	−63.2	−1.4	1.0	54.3	−0.7	0.5
59353.8973	0.234	55.6	0.7	1.0	−71.7	−4.2	0.5

Note.
[a] Phases have been computed with the Period (P) and Epoch (T) values of our new spectroscopic solution (Table 6).

(This table is available in its entirety in machine-readable form.)

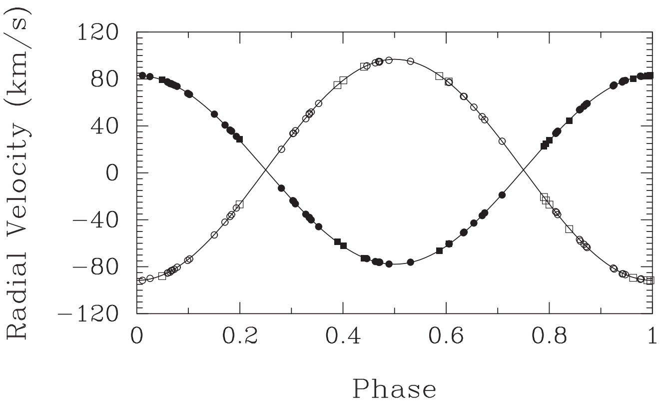

Figure 1. HD 71636 radial velocities (solid symbols = primary, open symbols = secondary) compared with the computed velocity curves (solid lines). Squares = KPNO, and circles = Fairborn Observatory. Phase zero is a time of maximum velocity for the primary.

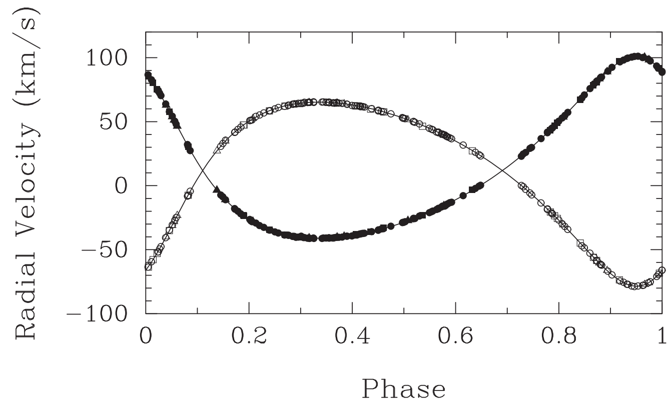

Figure 3. V1022 Cas radial velocities (solid symbols = primary, open symbols = secondary) compared with the computed velocity curves (solid lines). Squares = KPNO, triangles = McDonald Observatory, and circles = Fairborn Observatory. Phase zero is a time of periastron passage.

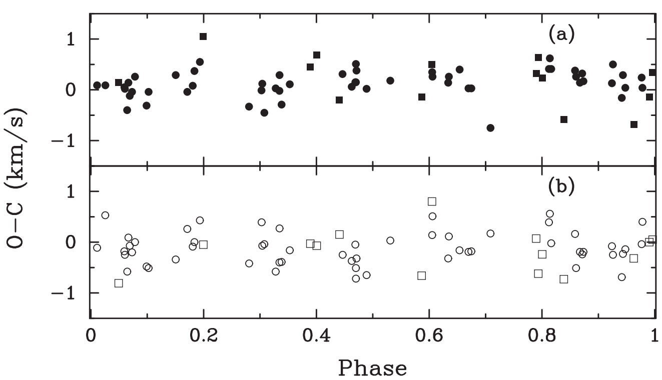

Figure 2. HD 71636 radial-velocity residuals, the observed minus computed velocities vs. orbital fractional phase for the primary, panel (a), and secondary, panel (b). Squares = KPNO, and circles = Fairborn Observatory.

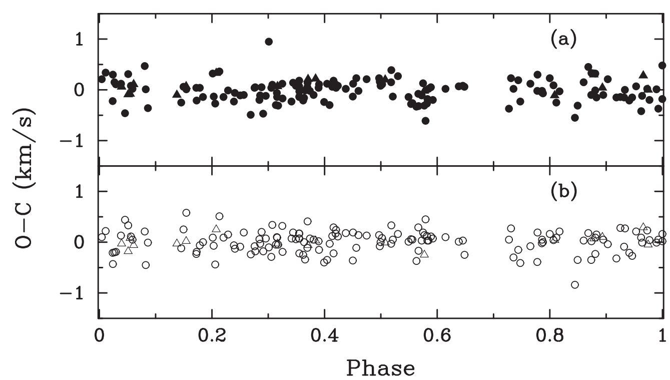

Figure 4. V1022 Cas radial-velocity residuals vs. orbital fractional phase for the primary, panel (a), and secondary, panel (b). Squares = KPNO, triangles = McDonald Observatory, and circles = Fairborn Observatory.

Table 4
HD 71636 Spectroscopic Orbital Elements and Related Parameters

Parameter	Henry et al. (2006) Value	This Study Value
P (days)	5.013289 ± 0.000035	5.0133144 ± 0.0000015
T_0 (HJD)	2,452,676.4610 ± 0.0018	2,457,419.05630 ± 0.00039
e	0.0 (adopted)	0.0 (adopted)
K_1 (km s^{-1})	80.33 ± 0.18	80.436 ± 0.054
K_2 (km s^{-1})	94.48 ± 0.19	94.223 ± 0.054
γ (km s^{-1})	2.573 ± 0.098	2.551 ± 0.029
$a_1 \sin i$ (10^6 km)	5.538 ± 0.013	5.5451 ± 0.0037
$a_2 \sin i$ (10^6 km)	6.513 ± 0.013	6.4955 ± 0.0037
$m_1 \sin^3 i$ ($M_\odot$)	1.5032 ± 0.0069	1.4931 ± 0.0020
$m_2 \sin^3 i$ ($M_\odot$)	1.2780 ± 0.0063	1.2746 ± 0.0018
Standard error of an observation of unit weight (km s^{-1})	0.5	0.3

Note. Solution computed from spectroscopic data alone with the binary orbit program SB2C.

Table 5
V1022 Cas Spectroscopic Orbital Elements and Related Parameters

Parameter	Value
P (days)	12.1561595 ± 0.0000025
T (HJD)	2,456,029.6120 ± 0.0013
e	0.31140 ± 0.00022
ω (deg)	34.469 ± 0.045
K_1 (km s^{-1})	71.121 ± 0.023
K_2 (km s^{-1})	71.942 ± 0.023
γ (km s^{-1})	11.776 ± 0.011
$a_1 \sin i$ (10^6 km)	11.2974 ± 0.0037
$a_2 \sin i$ (10^6 km)	11.4278 ± 0.0038
$m_1 \sin^3 i$ ($M_\odot$)	1.5915 ± 0.0011
$m_2 \sin^3 i$ ($M_\odot$)	1.5733 ± 0.0011
Standard error of an observation of unit weight (km s^{-1})	0.2

Note. Solution computed from spectroscopic data alone with binary orbit program SB2.

our group observing sequence to acquire 10 differential measurements of V1022 Cas minus the comparison star. All 10 of the resulting differential magnitudes in both filters were retained for analysis, and the group was repeated continuously. Our photometry confirms the shallow, partial eclipses suspected by Fekel et al. (2010). The extinction-corrected and transformed differential magnitudes in V and B are listed in Table 8. The orbital phases are based on the improved BV+TESS photometric ephemeris given in Table 15 of Section 5. The TESS observations came from two time

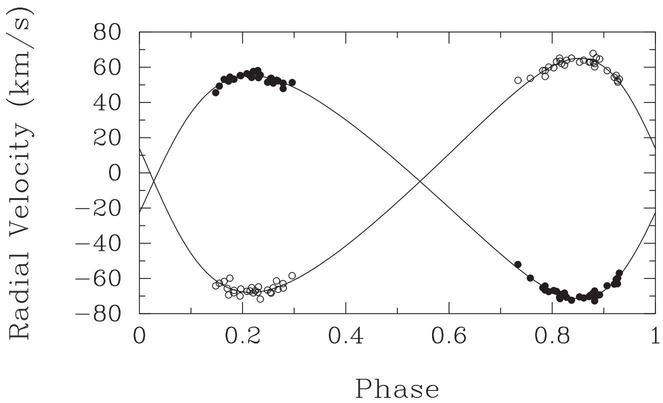

Figure 5. OT And radial velocities (solid symbols = primary, open symbols = secondary) compared with the computed velocity curves (solid lines). Phase zero is a time of periastron passage.

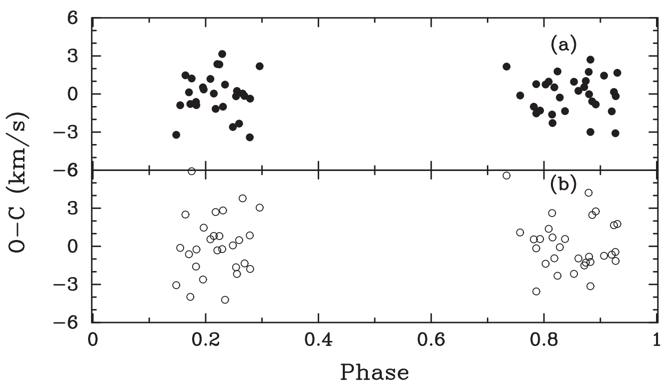

Figure 6. OT And radial-velocity residuals vs. orbital fractional phase for the primary, panel (a), and secondary, panel (b).

Table 6
OT And Spectroscopic Orbital Elements and Related Parameters

Parameter	Value
P (days)	20.85309 ± 0.00028
T (HJD)	2,456,304.459 ± 0.054
e	0.2240 ± 0.0051
ω (deg)	256.74 ± 0.91
K_1 (km s^{-1})	63.37 ± 0.23
K_2 (km s^{-1})	66.49 ± 0.32
γ (km s^{-1})	−4.84 ± 0.18
$a_1 \sin i$ (10^6 km)	17.709 ± 0.066
$a_2 \sin i$ (10^6 km)	18.583 ± 0.092
$m_1 \sin^3 i$ ($M_\odot$)	2.243 ± 0.023
$m_2 \sin^3 i$ ($M_\odot$)	2.137 ± 0.018
Standard error of an observation of unit weight (km s^{-1})	1.6

Note. Solution computed from spectroscopic data alone with binary orbit program SB2.

intervals: HJD 2,458,765 through HJD 2,458,787 and HJD 2,458,955 through HJD 2,458,981. The 3533 observations include four primary eclipses and three secondary ones.

4.3. OT And

We acquired 3446 new photometric observations of OT And in V and 3451 in B between 2013 May and 2018 June with the same procedure that is described above for V1022 Cas. We used HD 219109 as our comparison star. The extinction-corrected and transformed differential magnitudes in V and B are given in Table 9, along with the heliocentric Julian dates and the orbital phases computed with the refined BV+TESS photometric ephemeris given in Table 18 of Section 5. The 3879 TESS magnitudes cover three primary and one secondary eclipse from HJD 2,458,739 through HJD 2,458,787.

Table 7
Photometric Observations of HD 71636

Hel. Julian Date (HJD − 2,400,000)	Phase[a]	ΔV (Mag)	ΔB (Mag)
52539.9899	0.5282	1.993	1.299
52540.9877	0.7272	1.998	⋯
52542.9829	0.1252	1.993	1.308
52543.9817	0.3244	⋯	1.298

Notes. In Henry et al. (2006), the B and V column headers were reversed; they have been corrected in the present table. This table is presented in its entirety in machine-readable form.
[a] Phases have been computed with the BV+TESS ephemeris given in Table 12 of Section 5.

(This table is available in its entirety in machine-readable form.)

Table 8
Photometric Observations of V1022 Cas

Hel. Julian Date (HJD − 2,400,000)	Phase[a]	ΔV (Mag)	ΔB (Mag)
55175.7863	0.6789	−0.612	−1.160
55176.7373	0.7572	−0.611	−1.160
55199.5635	0.6349	−0.603	−1.158
55199.5674	0.6352	−0.602	−1.154

Note.
[a] Phases have been computed with the BV+TESS ephemeris given in Table 15 of Section 5.

(This table is available in its entirety in machine-readable form.)

Table 9
Photometric Observations of OT And

Hel. Julian Date (HJD − 2,400,000)	Phase[a]	ΔV (Mag)	ΔB (Mag)
56437.9403	0.3744	0.434	0.417
56438.9378	0.4222	⋯	0.435
56439.9345	0.4700	0.438	0.428
56441.9317	0.5658	0.421	0.435

Note.
[a] Phases have been computed with the BV+TESS ephemeris given in Table 18 of Section 5.

(This table is available in its entirety in machine-readable form.)

5. Combined Light and Velocity Solution

Combined light and velocity solutions were computed from our photometric and spectroscopic observations with the 2015 version of the Wilson–Devinney (WD) program. The physical model of that program is described in detail in Wilson & Devinney (1971), Wilson (1979), Wilson (1990), Wilson (2012a), Wilson (2012b), Van Hamme & Wilson (2007), Wilson et al. (2010), and Wilson & Van Hamme (2014). The three eclipsing systems are detached, so we used mode 2 of the WD program in each case. All observations in each data set were assigned a weight of unity. Curve-dependent weights were initially based on the standard deviations for the whole curves, listed in Table 10, and were then subsequently updated by the software. Light-level-dependent weights were applied inversely proportional to the square root of the light level. We used the square-root limb-darkening law with the x, y coefficients from Van Hamme (1993). The values of our nonvarying bolometric albedo, gravity-darkening, and limb-darkening coefficients are provided in Table 11 for each of the three systems. To obtain the derived physical properties, we used the nominal values of the solar quantities defined by IAU 2015 Resolution B3 (Prsa et al. 2016).

5.1. HD 71636

The orbital elements from our spectroscopic solution were adopted as starting values for the combined WD solution. The spectrum addition fit of Henry et al. (2006) resulted in F2 V and F5 V spectral types. Given the early- and mid-F spectral types of the components, the gravity-darkening (g) and bolometric albedo (A) coefficients were fixed at canonical values for convective outer layers (Lucy 1967). We assumed that the orbit is circular. The period was allowed to vary, but the results did not indicate that this was the case. We also investigated the possibility of small amounts of third light, but the WD software always preferred zero values for both passbands. The detailed reflection effect option, with two reflections, was employed.

To estimate the surface temperature of the primary star, we examined previous analyses. For the combined HD 71636 system, Masana et al. (2006) found 6772 K from V and Two Micron All Sky Survey photometry, while Casagrande et al. (2011) determined a nearly identical temperature of 6776 K from the IR flux method. These results indicate that the primary's temperature should be greater than 6775 K, since Henry et al. (2006) estimated a ΔV of 0.6 ± 0.1 mag between the components from a fit of the spectrum with two reference stars. Given the above results for the primary component, we adopt a temperature of 6950 K, the same as that used by Henry et al. (2006).

Our final best-fit solutions using our radial velocities with first the B and V photometry, then with the TESS observations, and lastly with all of the photometry are given in Table 12. Unless specifically noted, all of the presented "final" solution results are based on the solution with the three photometric sets. The listed uncertainties are standard deviations taken directly from the final WD solution. When compared with the ground-based results, the analysis of the more precise TESS data produces a significant reduction in the uncertainties for several of the parameters (Table 12). Adopted parameter values are labeled as such. Due to the questions raised by Maxted et al. (2020) regarding the formal errors computed by the WD software, we ran a Monte Carlo–like series of simulations to provide errors for the computed absolute dimensions. Using a simple Gaussian distribution centered on our final result, we varied the initial values of the inclination, both surface potentials, both temperatures, and the mass ratio. During the 405 WD runs, all of these parameters were adjusted, except for the randomly-assigned temperature of the primary star. The larger values of either the standard deviations from these runs

Table 10
Measurement Characteristics

Data Type	Data Points	Normal Mag	Std. Dev.[a]
HD 71636			
Johnson V	717	+1.999	0.005
Johnson B	729	+1.301	0.004
TESS	1983	+1.002	0.001
RV_1	70	⋯	0.32 km s^{-1}
RV_2	70	⋯	0.39 km s^{-1}
V1022 Cas			
Johnson V	1421	−0.606	0.004
Johnson B	1422	−1.157	0.004
TESS	3533	+0.628	0.001
RV_1	189	⋯	0.23 km s^{-1}
RV_2	189	⋯	0.22 km s^{-1}
OT And			
Johnson V	3446	+0.430	0.004
Johnson B	3451	+0.425	0.004
TESS (Set 1)	2074	+0.629	0.001
TESS (Set 2)	1805	+0.645	0.001
RV_1	57	⋯	1.69 km s^{-1}
RV_2	57	⋯	2.61 km s^{-1}

Note.
[a] For the light curves, in units of total light at phase $0\overset{\text{p}}{.}25$.

Table 11
Nonvarying WD Parameters

Parameter	Symbol	Value
HD 71636		
Albedo (bol)	A_1, A_2	0.500, 0.500
Gravity darkening	g_1, g_2	0.300, 0.300
Limb darkening (bol)	x_1, y_1	+0.086, +0.638
Limb darkening (bol)	x_2, y_2	+0.116, +0.603
Limb darkening (V)	x_1, y_1	+0.063, +0.724
Limb darkening (V)	x_2, y_2	+0.115, +0.687
Limb darkening (B)	x_1, y_1	+0.191, +0.691
Limb darkening (B)	x_2, y_2	+0.303, +0.580
Limb darkening (TESS)	x_2, y_2	−0.069, +0.716
Limb darkening (TESS)	x_2, y_2	−0.028, +0.695
V1022 Cas		
Albedo (bol)	A_1, A_2	0.500, 0.500
Gravity darkening	g_1, g_2	0.300, 0.300
Limb darkening (bol)	x_1, y_1	+0.116, +0.603
Limb darkening (bol)	x_2, y_2	+0.116, +0.603
Limb darkening (V)	x_1, y_1	+0.115, +0.687
Limb darkening (V)	x_2, y_2	+0.115, +0.687
Limb darkening (B)	x_1, y_1	+0.303, +0.580
Limb darkening (B)	x_2, y_2	+0.303, +0.580
Limb darkening (TESS)	x_2, y_2	−0.004, +0.686
Limb darkening (TESS)	x_2, y_2	−0.028, +0.695
OT And		
Albedo (bol)	A_1, A_2	1.000, 1.000
Gravity darkening	g_1, g_2	1.000, 1.000
Limb darkening (bol)	x_1, y_1	+0.248, +0.488
Limb darkening (bol)	x_2, y_2	+0.309, +0.410
Limb darkening (V)	x_1, y_1	+0.081, +0.727
Limb darkening (V)	x_2, y_2	+0.085, +0.703
Limb darkening (B)	x_1, y_1	+0.093, +0.838
Limb darkening (B)	x_2, y_2	+0.139, +0.765
Limb darkening (TESS)	x_2, y_2	−0.037, +0.652
Limb darkening (TESS)	x_2, y_2	−0.009, +0.610

Table 12
HD 71636 Light and Velocity Curve Results[a]

Parameter	BV Only	TESS Only	BV and TESS
Period (days)	5.01331290 ± 0.000000023	5.01331392 ± 0.00000059	5.01331360 ± 0.00000009
Epoch[b] (HJD)	2,452,677.71503 ± 0.00012	2,452,677.71454 ± 0.00081	2,452,677.71499 ± 0.00012
Eccentricity	0 (adopted)	0 (adopted)	0 (adopted)
System velocity (km s^{-1})	2.583 ± 0.030	2.576 ± 0.030	2.590 ± 0.030
Temperature 1 (K)	6950 (adopted)	6950 (adopted)	6950 (adopted)
Temperature 2 (K)[c]	6438 ± 5	6442 ± 1	6442 ± 1
Potential 1	12.203 ± 0.153	11.877 ± 0.015	11.836 ± 0.014
Potential 2	11.627 ± 0.179	12.089 ± 0.025	12.155 ± 0.022
Inclination (deg)	85.577 ± 0.038	85.718 ± 0.005	85.743 ± 0.005
Semimajor axis ($R_\odot$)	17.355 ± 0.008	17.351 ± 0.008	17.353 ± 0.008
Mass ratio	0.8530 ± 0.0008	0.8528 ± 0.0003	0.8511 ± 0.0003
Luminosity ratio (V)			0.6599 ± 0.0015
Luminosity ratio (B)			0.6826 ± 0.0015
Luminosity ratio (TESS)			0.6394 ± 0.0015

Notes.
[a] Wilson–Devinney simultaneous solution, including proximity and eclipse effects, of the light and velocity data.
[b] Minimum of primary eclipse.
[c] The uncertainty provided by the WD solution is the uncertainty of the difference in temperature between the primary and secondary.

Table 13
Fundamental Parameters of HD 71636

Parameter	Primary Star	Secondary Star
M ($M_\odot$)	1.506 ± 0.002	1.282 ± 0.002
R ($R_\odot$)	1.583 ± 0.024	1.314 ± 0.030
$L/L_\odot$	5.26 ± 0.44	2.68 ± 0.25
$M_{\rm bol}$	2.94 ± 0.21	3.67 ± 0.23
log g (cm s^{-2})	4.22 ± 0.01	4.31 ± 0.02
T (K)	6950 ± 140	6443 ± 140

or from the direct error propagation of the absolute dimension calculations are shown in Table 13.

The primary characteristics of the two stars are representative of mid-F main-sequence stars. The masses are $M_1 = 1.506 \pm 0.002\,M_\odot$ and $M_2 = 1.282 \pm 0.002\,M_\odot$, whereas the equal-volume radii are $R_1 = 1.583 \pm 0.024\,R_\odot$ and $R_2 = 1.314 \pm 0.030\,R_\odot$ for the primary and secondary, respectively. The effective temperatures are 6950 K for the primary and 6443 K for the secondary. We adopt the temperature errors of Henry et al. (2006), which are ±140 K for both stars. The orbital inclination is $85\fdg74 \pm 0\fdg01$.

To examine this WD solution, we compared our derived stellar brightness results with the observed combined V magnitude of the system. We initially computed the $M_{\rm bol}$ values using our temperatures and radii in the Stefan–Boltzmann equation (see Table 13). For the error bars, we used the WD radii results and our assumed $\Delta T = \pm 140$ K. From our final combined WD solution, the calculated luminosities are $5.26 \pm 0.44\ L_\odot$ and $2.68 \pm 0.25\ L_\odot$, and the bolometric magnitudes are $M_{\rm bol} = 2.94 \pm 0.21$ mag and $M_{\rm bol} = 3.67 \pm 0.23$ mag for the primary and secondary, respectively. The Gaia Early Data Release 3 (EDR3) parallax of HD 71636 is $0\farcs008430 \pm 0\farcs000031$ (Gaia Collaboration et al. 2021) and corresponds to a distance of 118.6 ± 0.4 pc. Utilizing the bolometric correction from Flower (1996) for both stars and the Gaia distance, we obtain $V_1 = 8.28 \pm 0.14$ mag and $V_2 = 9.04 \pm 0.14$ mag for the two components. These individual magnitudes combine to give a brightness for the system of $V = 7.84 \pm 0.19$ mag. Green et al. (2019) indicate a

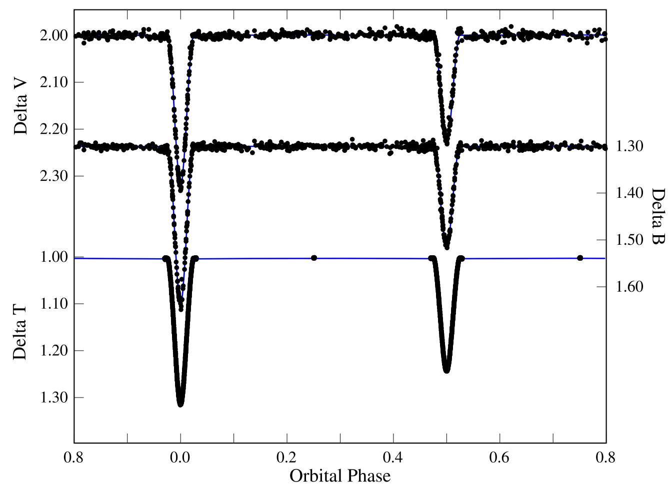

Figure 7. The differential Johnson BV magnitudes from Fairborn and the TESS magnitudes fitted with the Wilson–Devinney solution curves for HD 71636. Phases were computed with the BV+TESS ephemeris in Table 12.

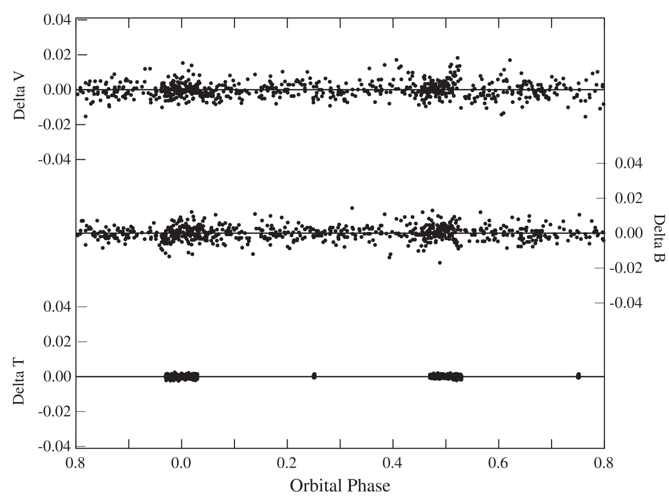

Figure 8. The residuals of the HD 71636 photometry from the light-curve solutions.

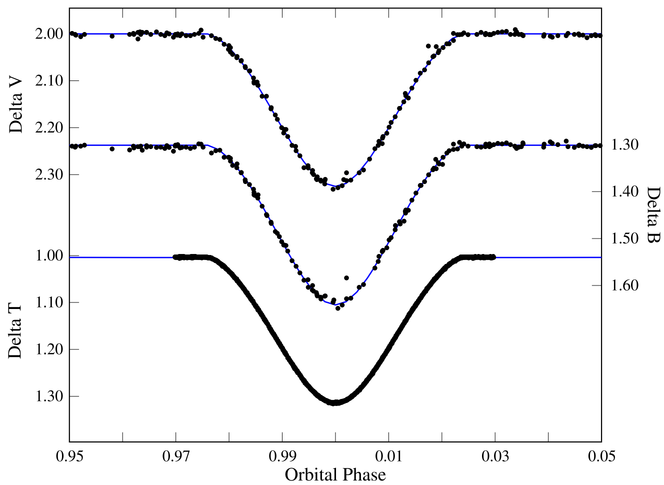

Figure 9. An enlarged view of the HD 71636 primary eclipse.

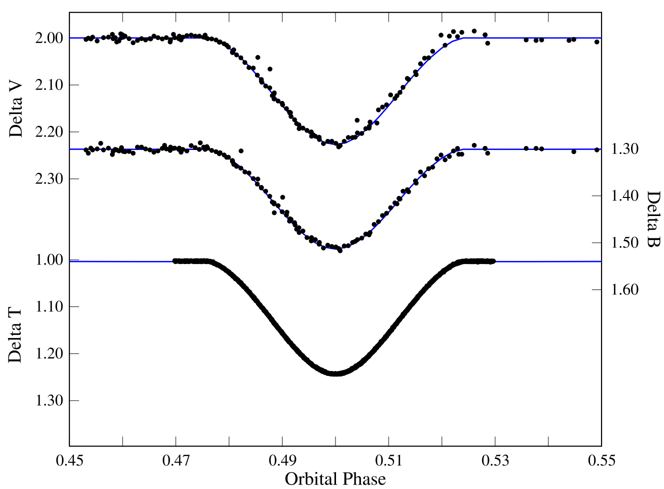

Figure 10. An enlarged view of the HD 71636 secondary eclipse.

small color excess of $E(B-V)=0.01$, resulting in a reddening of $A_V=0.03$ mag, which would increase the combined computed V magnitude to 7.87 ± 0.19. We note that the converted Tycho (Høg et al. 2000) to Johnson V magnitude for HD 71636 is 7.90 ± 0.01 mag, so there is very good agreement with the result produced from our adopted solution.

The three photometric data sets are plotted with the light-curve solution in Figure 7 and the residuals to the fits are shown in Figure 8. Expanded views of the primary and secondary eclipses are provided in Figures 9 and 10, respectively.

The ephemeris for the primary eclipse of HD 71636 is

$$\text{Minimum Light (HJD)} = 2{,}452{,}677.71499 \pm 0.00012 + 5.01331360 \pm 0.00000009\ \text{E}.$$

From the orbital elements P and T_0, listed in Table 4, the ephemeris for maximum velocity compares very well with the combined solution. The periods are almost identical, and the difference in T_0 is equal to 0.250 units in phase.

The WD program provides geometrical information about the two components. Relative radii are given in four directions: from the center toward the poles, toward the sides, toward the back (i.e., away from the companion), and toward the inner Lagrangian point, L1. These parameter values are listed in Table 14 along with their standard deviations from the final

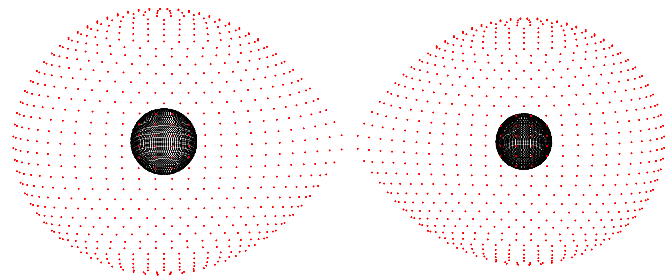

Figure 11. An image of HD 71636 at phase 0.25. The Roche lobes were computed by changing to the mode 6 option, and that solution is plotted in red.

Table 14
Model Radii of HD 71636

Parameter	Value
r_1 (pole)	0.0910 ± 0.0001
r_1 (point)	0.0911 ± 0.0001
r_1 (side)	0.0910 ± 0.0001
r_1 (back)	0.0911 ± 0.0001
r_2 (pole)	0.0769 ± 0.0001
r_2 (point)	0.0770 ± 0.0001
r_2 (side)	0.0769 ± 0.0001
r_2 (back)	0.0770 ± 0.0001

WD solution. It is seen that for both components the four directional radii are essentially the same, so the stars are spherically shaped. Comparing the radii of the components between the mode 2 (detached) and mode 6 (contact) options in the WD program, the radii of the primary and secondary are 25% and 19%, respectively, of their Roche lobe radii (see Figure 11). Consequently, HD 71636 is a well-detached system even though it is a rather close binary.

5.2. V1022 Cas

Given the mid-F spectral types for the components of V1022 Cas, we assumed that the outer envelopes of both stars are convective and used the corresponding gravity-darkening, g, and bolometric albedo, A, coefficients from Lucy (1967). Because of the eccentric orbit, the simple one-reflection option (Wilson 1990) was employed. We examined the possibilities of third light and a variable period, but our WD solutions found no significant evidence for either one. We note that because the masses of the two stars are similar, the slightly more massive star is the more evolved of the two, and so it is the cooler and larger component.

In the recent analysis of Lester et al. (2019), they derived a temperature of 6450 ± 120 K for the primary and 6590 ± 110 K for the secondary by reconstructing the spectrum of each component. Adopting their effective temperature of 6450 K for the primary, the WD solution of our data, as expected, produced a hotter temperature for the secondary, 6544 K, but resulted in a secondary that was 0.05 mag brighter than the primary. Thus, we reviewed spectral classifications and photometric indices for additional guidance in determining the temperature of the primary star. The best spectral classifications are F5 IVn from W. W. Morgan (Abt & Bidelman 1969), F6 V by Cowley (1976), and a more recent one of F6 V by Abt (2009). From SIMBAD's basic data section, Høg et al. (2000) provided a combined system $B-V$ of 0.47. This color corresponds to a temperature of 6409 K from Flower (1996), 6312 K from

Table 15
V1022 Cas Light and Velocity Curve Results[a]

Parameter	BV Only	TESS Only	BV and TESS
Period (days)	12.1561585 ± 0.0000010	12.1561601 ± 0.0000008	12.1561594 ± 0.0000006
Epoch[b] (HJD)	2,453,295.48471 ± 0.00027	2,453,295.48487 ± 0.00021	2,453,295.48476 ± 0.00017
Eccentricity	0.3115 ± 0.0001	0.3115 ± 0.0001	0.3115 ± 0.0001
Periastron angle (deg)	34.464 ± 0.018	34.472 ± 0.014	34.468 ± 0.012
System velocity (km s^{-1})	11.769 ± 0.005	11.768 ± 0.004	11.769 ± 0.003
Temperature 1 (K)	6350 (adopted)	6350 (adopted)	6350 (adopted)
Temperature 2 (K)[c]	6418 ± 33	6389 ± 32	6420 ± 15
Potential 1	14.145 ± 0.236	14.064 ± 0.161	14.083 ± 0.114
Potential 2	14.895 ± 0.169	14.684 ± 0.126	14.802 ± 0.085
Inclination (deg)	82.958 ± 0.063	82.884 ± 0.038	82.925 ± 0.025
Semimajor Axis ($R_\odot$)	32.901 ± 0.005	32.906 ± 0.004	32.903 ± 0.003
Mass ratio	0.9885 ± 0.0002	0.9885 ± 0.0001	0.9885 ± 0.0001
Luminosity ratio (V)			0.5212 ± 0.0086
Luminosity ratio (B)			0.5176 ± 0.0092
Luminosity ratio (TESS)			0.5225 ± 0.0081

Notes.
[a] Wilson–Devinney simultaneous solution, including proximity and eclipse effects, of the light and velocity data.
[b] Minimum of primary eclipse.
[c] The uncertainty provided by the WD solution is the uncertainty of the difference in temperature between the primary and secondary.

Gray (1992), and 6339 K from Eker et al. (2018), and spectral classes of F6 in the latter two references. From Paunzen (2015) the average $b - y$ is 0.313 and β is 2.650. According to the scale of Crawford (1975b), this Hβ value corresponds to an F6 V spectral type, indicating that there is little or no reddening. While both Lester et al. (2019) and Southworth (2021) adopted $E(B - V) = 0.04$, given the above photometric results and a distance of just 63.63 ± 0.18 pc from the Gaia EDR3 parallax (Gaia Collaboration et al. 2021), we assume that there is no color excess, and so the interstellar extinction is zero. Fekel et al. (2010) found a magnitude difference between the components of only about 0.1 mag, and the results of Lester et al. (2019) and Southworth (2021) indicate an even smaller magnitude difference, so only a very modest temperature difference between the two stars is expected. Guided by the photometric calibrations, for the primary we chose to adopt a temperature of 6350 K, which is still within the uncertainty of the value of Lester et al. (2019), and which produced a more consistent solution. An uncertainty of ±150 K was assumed for both the primary and secondary in our discussion and comparisons of observational and theoretical results.

The orbital elements from our spectroscopic solution were adopted as starting values for our combined WD solutions. Once again we obtained three separate solutions: first the radial velocities were combined with the ground-based photometry, then with the TESS observations, and lastly with all of the photometry. As is seen in Table 15, when compared with the ground-based results, the analysis of the more precise TESS data produces a modest improvement in the uncertainties for some of the parameters. After the final solution was derived, a Monte Carlo simulation, similar to that previously described, was performed. The WD solution resulted in masses of $M_1 = 1.626 \pm 0.001\, M_\odot$ and $M_2 = 1.607 \pm 0.001\, M_\odot$, and equal-volume radii of $R_1 = 2.570 \pm 0.021\, R_\odot$ and $R_2 = 2.445 \pm 0.022\, R_\odot$ for the primary and secondary, respectively. The effective temperatures, T_1 and T_2, and their assumed errors are 6350 ± 150 K and 6420 ± 150 K, respectively, for a difference of just 70 K. The system's inclination is 82.°92 ± 0.°02. The complete WD solution of the combined spectroscopic and

Table 16
Fundamental Parameters of V1022 Cas

Parameter	Primary	Secondary
M ($M_\odot$)	1.626 ± 0.001	1.607 ± 0.001
R ($R_\odot$)	2.570 ± 0.021	2.445 ± 0.022
$L/L_\odot$	9.67 ± 1.08	9.15 ± 0.97
$M_{\rm bol}$ (mag)	2.28 ± 0.28	2.34 ± 0.27
$\log g$ (cm s^{-2})	3.83 ± 0.02	3.87 ± 0.01
T (K)	6350 ± 150	6420 ± 150

photometric data is given in Table 15, and the list of absolute dimensions is in Table 16.

To examine this WD solution, we compared our derived stellar brightness results with the Gaia EDR3 distance and the observed combined V magnitude of the system. We initially computed the $M_{\rm bol}$ values using our temperatures and radii in the Stefan–Boltzmann equation (see Table 16). For the error bars, we used the WD radii results and our assumed $\Delta T = \pm 150$ K. From our final combined WD solution, the calculated luminosities are $9.67 \pm 1.08\ L_\odot$ and $9.15 \pm 0.97\ L_\odot$, which result in bolometric magnitudes of $M_{\rm bol} = 2.28 \pm 0.28$ mag and $M_{\rm bol} = 2.34 \pm 0.27$ mag for the primary and secondary, respectively. The Gaia EDR3 parallax of V1022Cas is 0.″015717 ± 0.″000046 (Gaia Collaboration et al. 2021) and corresponds to a distance of 63.63 ± 0.18 pc. Utilizing the bolometric correction from Flower (1996) for both stars and the Gaia distance, we obtain $V_1 = 6.30 \pm 0.19$ mag and $V_2 = 6.36 \pm 0.19$ mag for the two components. These individual magnitudes combine to give a brightness for the system of $V = 5.57 \pm 0.26$ mag. We note that the converted Tycho (Høg et al. 2000) to Johnson V magnitude for V1022 Cas is 5.56 ±0.01 mag, so there is excellent agreement with the result produced from our adopted solution.

The observational photometric data are plotted with the light-curve solution in Figure 12. The deeper eclipse, which for V1022 Cas is when the more massive but cooler star is eclipsed by the less massive but hotter star, is plotted at phase zero. The residuals to the fits are shown in Figure 13. The primary and

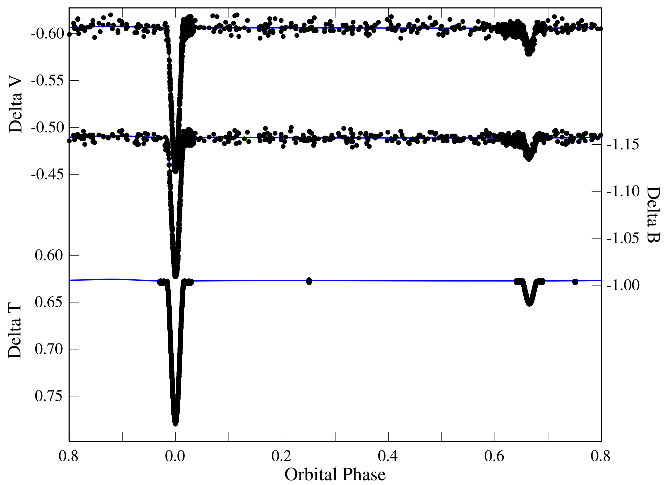

Figure 12. The differential Johnson *BV* magnitudes of V1022 Cas obtained at the Fairborn Observatory during 2009–2018 and the TESS data, all of which are fitted with the Wilson–Devinney solution curves. Phases were computed with the BV+TESS ephemeris in Table 15.

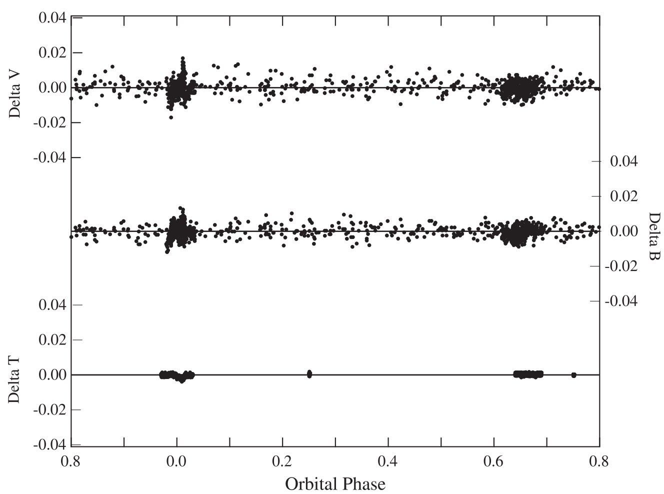

Figure 13. The residuals of the fits of the solution curves and observations of V1022 Cas.

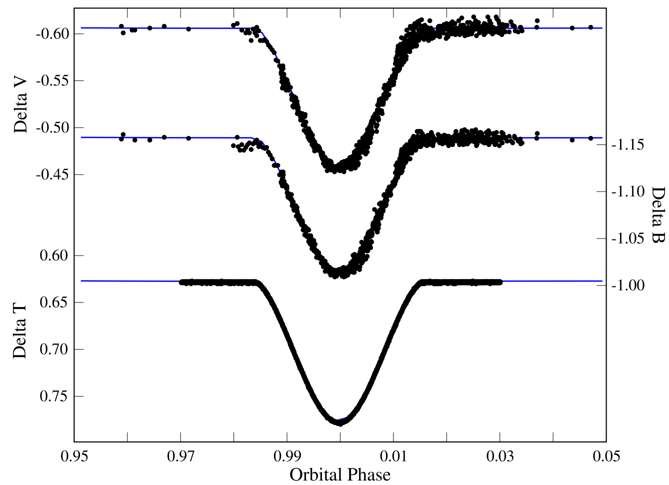

Figure 14. An expanded view of the primary eclipse of V1022 Cas.

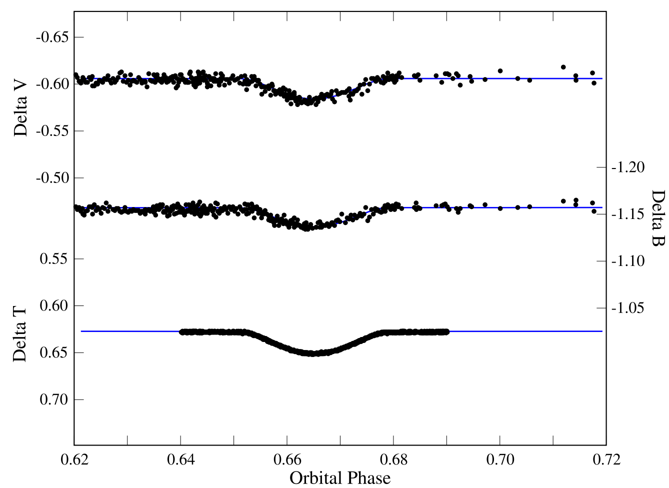

Figure 15. An expanded view of the secondary eclipse of V1022 Cas.

secondary eclipses are provided in Figures 14 and 15, respectively.

Our refined ephemeris is

$$\text{Minimum Light (HJD)} = 2{,}453{,}295.48476 \pm 0.00017 + 12.1561594 \pm 0.0000006\,E.$$

This photometric period is in excellent agreement with our spectroscopic value of 12.1561595 ± 0.0000025 days.

With the use of the WD program, our Figure 16 shows the sizes of the stars (see the relative radii listed in Table 17) relative to their Roche lobes at a time of periastron. The Roche lobes of the two components were computed by utilizing mode 6 of the WD program. Both components are spherical and the stellar radii are 21% and 20% the size of the Roche lobe radii.

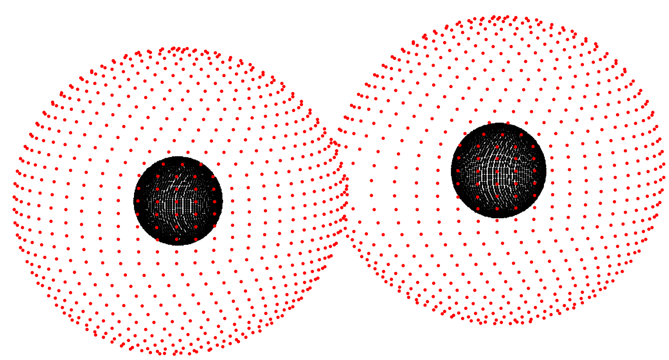

Figure 16. An image of V1022 Cas at periastron. The Roche lobes were computed by changing to the mode 6 option, and that solution is plotted in red.

5.3. *OT And*

Once again, the orbital elements from our spectroscopic solution were adopted as starting values for our combined WD solution. Given the A spectral types of the components, the gravity-darkening (g) and bolometric albedo (A) coefficients were fixed at canonical values for radiative outer layers (Lucy 1967) and are shown in Table 11. As in the case of V1022 Cas and its eccentric orbit, we employed the simple one-reflection option (Wilson 1990). We also examined the possibilities of third light and a variable period, but our WD solutions found no significant evidence for either one. Since the components of OT And have such similar masses, the more massive star, which we identify as the primary, is slightly more evolved and hence slightly cooler than the secondary.

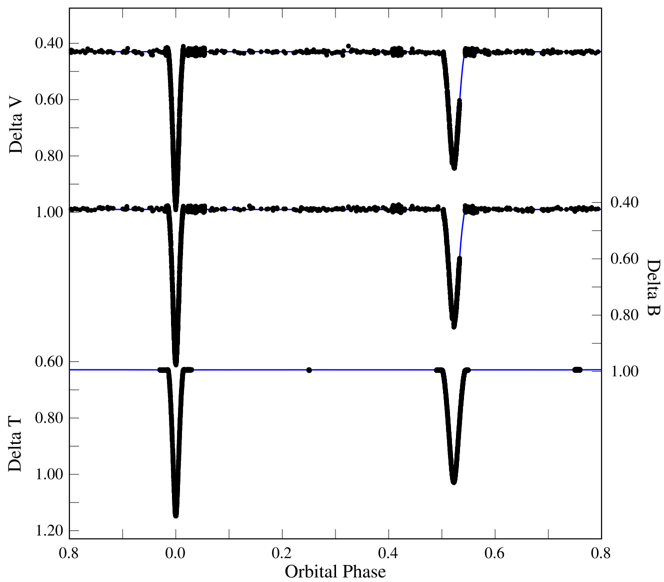

Figure 17. The differential Johnson *BV* magnitudes of OT And obtained at the Fairborn Observatory during 2013–2018 and the TESS data, which are fitted with the Wilson–Devinney solution curves. Phases were computed with the BV+TESS ephemeris in Table 18.

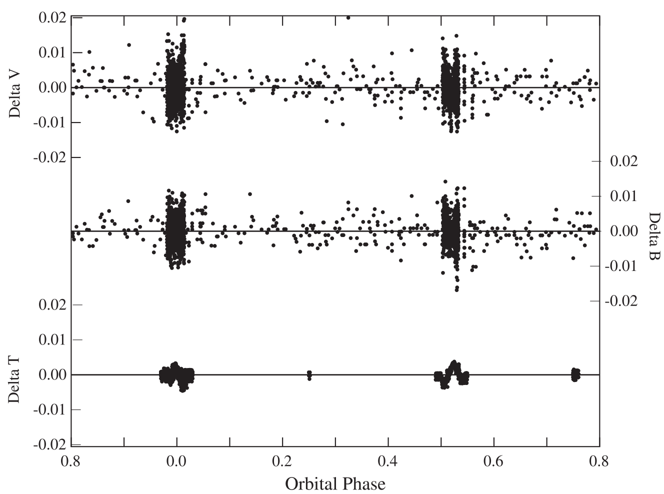

Figure 18. The residuals of the fits of the solution curves and observations of OT And.

To determine the temperature of the primary, we started with the observed combined $B-V$, listed in SIMBAD as 0.21 from Tycho observations (Høg et al. 2000). The Gaia EDR3 parallax of $0\farcs004082 \pm 0\farcs000023$ (Gaia Collaboration et al. 2021) corresponds to a distance of 245.0 ± 1.4 pc, a distance that indicates that the system's $B - V$ color is reddened. From Green et al. (2019), we find $E(B-V) = 0.064$ mag, which results in $(B-V)_0 = 0.15$ for the combined system. This color corresponds to an effective temperature of 7826 K from Gray (1992), 8083 K from Flower (1996), and 8222 K from Eker et al. (2018). From our spectroscopic observations, we estimate a magnitude difference of just 0.4 mag, suggesting only a modest temperature difference between the two stars. As the primary is the cooler star, we adopt a temperature of 8000 K.

Once again we obtained three separate solutions: first the radial velocities were combined with the ground-based photometry, then with the TESS observations, and lastly with all of the photometry. As is seen in Table 18, when compared with the ground-based results, the analysis of the more precise TESS data produces a modest reduction in the uncertainties of several of the parameters. Our final WD solution using both the ground-based and TESS photometry with the effective temperature of the primary, T_1, fixed at 8000 K results in masses of $M_1 = 2.253 \pm 0.014\,M_\odot$ and $M_2 = 2.147 \pm 0.011\,M_\odot$, and equal-volume radii of $R_1 = 3.167 \pm 0.013\,R_\odot$ and $R_2 = 2.649 \pm 0.015\,R_\odot$ for the primary and secondary, respectively. The effective temperature for the hotter secondary is $T_2 = 8156$ K. We estimate temperature errors of ± 200 K for both components. The other standard deviations for the absolute dimensions are via our Monte Carlo simulation technique. The system's inclination is $88\fdg40 \pm 0\fdg01$. The full WD solution and absolute dimensions are given in Tables 18 and 19, respectively.

Table 17
Model Radii of V1022 Cas

Parameter	Value
r_1 (pole)	0.0790 ± 0.0007
r_1 (point)	0.0793 ± 0.0007
r_1 (side)	0.0791 ± 0.0007
r_1 (back)	0.0792 ± 0.0007
r_2 (pole)	0.0739 ± 0.0005
r_2 (point)	0.0741 ± 0.0005
r_2 (side)	0.0740 ± 0.0005
r_2 (back)	0.0741 ± 0.0005

As we did for V1022 Cas, we compare the computed and observed V magnitudes. With the Stefan–Boltzmann equation the temperatures with the adopted ± 200 K uncertainties and radii for OT And in Table 19 produce luminosities of $37.0 \pm 3.9\,L_\odot$ and $28.0 \pm 3.0\,L_\odot$ for the primary and secondary, respectively. Those values result in bolometric magnitudes $M_{\rm bol} = 0.82 \pm 0.26$ mag and $M_{\rm bol} = 1.12 \pm 0.26$ mag for the primary and secondary. Utilizing the bolometric corrections from Flower (1996) and the Gaia EDR3 distance of 245.0 ± 1.4 pc, we obtain $V_1 = 7.74 \pm 0.09$ mag and $V_2 = 8.05 \pm 0.09$ mag for the two components. The combined magnitude for the system is then $V = 7.13 \pm 0.13$ mag. With the color excess of 0.064 mag from Green et al. (2019), the corresponding visual extinction A_V is 0.20 mag. This results in an extinction-corrected magnitude of 7.33 ± 0.13, in good agreement with the V mag of 7.35 ± 0.01 listed in SIMBAD.

The light curves, the residuals, and the expanded views of the primary and secondary eclipses are shown in Figures 17 through 20. The deeper eclipse, which for OT And occurs when the less massive but hotter star is eclipsed by the more massive but cooler star, is plotted at phase zero.

The new photometric ephemeris for primary eclipse is

$$\begin{aligned}\text{Minimum Light (HJD)} = {} & 2{,}455{,}887.95865 \pm 0.00011 \\ & + 20.8529215 \pm 0.0000001\ \text{E}.\end{aligned}$$

This photometric period is in excellent agreement with our spectroscopic value of 20.85309 ± 0.00028 days.

Periastron passage for OT And occurs almost exactly at the time when the less massive but hotter star is eclipsed by the more massive but cooler star. So instead of displaying that phase to show the size of the components relative to their Roche lobes, in Figure 21 we compare the stellar radii listed in Table 20 with their Roche lobes at an orbital phase that is 0.08 from periastron. Both components are spherical, with the radius

Table 18
OT And Light and Velocity Curve Results[a]

Parameter	BV Only	TESS Only	BV and TESS
Period (days)	20.8529039 ± 0.00000316	20.8528733 ± 0.0000264	20.8529215 ± 0.0000010
Epoch[b] (HJD)	2,455,887.95966 ± 0.00027	2,455,887.96453 ± 0.00365	2,455,887.95865 ± 0.00011
Eccentricity	0.2113 ± 0.0004	0.2168 ± 0.0002	0.2149 ± 0.0002
Periastron angle (deg)	260.609 ± 0.022	260.878 ± 0.009	260.772 ± 0.012
System velocity (km s^{-1})	−5.170 ± 0.099	−5.161 ± 0.035	−5.161 ± 0.075
Temperature 1 (K)	8000 (adopted)	8000 (adopted)	8000 (adopted)
Temperature 2 (K)[c]	8159 ± 4	8132 ± 3	8156 ± 2
Potential 1	17.306 ± 0.026	17.345 ± 0.017	17.298 ± 0.013
Potential 2	19.593 ± 0.068	19.270 ± 0.033	19.628 ± 0.047
Inclination (deg)	88.418 ± 0.004	88.338 ± 0.002	88.399 ± 0.002
Semimajor axis ($R_\odot$)	52.342 ± 0.089	52.235 ± 0.032	52.253 ± 0.067
Mass ratio	0.9489 ± 0.0026	0.9525 ± 0.0011	0.9531 ± 0.0020
Luminosity ratio (V)			0.5718 ± 0.0008
Luminosity ratio (B)			0.5697 ± 0.0008
Luminosity ratio (TESS)			0.5776 ± 0.0008
Time of minimum[d]			2,451,425.4354 ± 0.0020
Time of minimum[e]			2,451,853.3856 ± 0.0007

Notes.
[a] Wilson–Devinney simultaneous solution, including proximity and eclipse effects, of the light and velocity data.
[b] Minimum of primary eclipse.
[c] The uncertainty provided by the WD solution is the uncertainty of the difference in temperature between the primary and secondary.
[d] Agerer & Hübscher (2001).
[e] Agerer & Hübscher (2003).

of the more massive star being 16% of its Roche lobe radius and the radius of the less massive star being 13%.

6. Discussion

6.1. HD 71636

As noted earlier, both Henry et al. (2006) and Clausen et al. (2010) were unable to find a consistent fit between the observationally determined properties of the two stars and evolutionary tracks. Clausen et al. (2010) concluded the likely problem was that the photometry of Henry et al. (2006) poorly covered secondary eclipse. Table 21 lists the masses, radii, temperatures, and luminosities of Henry et al. (2006) and our new solution. That comparison shows that our new values of the radius and luminosity of the secondary are somewhat reduced.

Because HD 71636 is a well-detached system and both stars are dwarfs, it is reasonable to assume that there has been no exchange or loss of mass and that the stars' evolutionary states can be estimated from single-star evolutionary models. The masses of the two stars are the most well determined of the basic parameters, having uncertainties of just 0.1% and 0.2% for the primary and secondary, respectively. Thus, in Figure 22 using our determined values of the parameters of the components (Table 13), we show mass–effective temperature and mass–radius diagrams, comparing our results with the stellar evolution models from the Isochrones and Stellar Tracks series (MIST; Choi et al. 2016), which is based on the Modules for Experiments in Stellar Astrophysics package (MESA; Paxton et al. 2011, 2013, 2015). The solid black lines are the model isochrones, which increase in age from bottom to top, ranging between 0.6 and 1.2 Gyr in steps of 0.2 Gyr. The best-fit age of 0.9 Gyr is shown by the solid blue line. The metallicity for this comparison is $[Fe/H] = 0.12$, which is the abundance that provides the best match to the effective temperatures. From the various fits, we estimate an abundance uncertainty of ±0.02. At an age of 0.9 Gyr, both stars are relatively close to the zero-age main sequence.

Table 19
Fundamental Parameters of OT And

Parameter	Primary	Secondary
M ($M_\odot$)	2.253 ± 0.014	2.147 ± 0.011
R ($R_\odot$)	3.167 ± 0.013	2.649 ± 0.015
$L/L_\odot$	37.0 ± 3.9	28.0 ± 3.0
M_{bol} (mag)	0.82 ± 0.26	1.12 ± 0.27
$\log g$ (cm s^{-2})	3.79 ± 0.01	3.92 ± 0.01
T (K)	8000 ± 200	8156 ± 200

Our WD solution significantly improves the agreement of the basic parameters of the components and provides a consistent age. Our new results supersede those of Henry et al. (2006), which Torres et al. (2010) listed in their compilation of eclipsing systems with well-determined parameters. It also enables the system's inclusion in future collective examinations of core overshoot.

6.2. V1022 Cas

With the solution of our radial velocities in combination with our ground-based and TESS photometry, there are now three different analyses of the basic properties of V1022 Cas. Of the other two, Lester et al. (2019) performed an analysis of V1022 Cas using radial-velocity and interferometric measurements. They derived the basic properties of the components including masses, radii, and temperatures. Their determination of the stellar radii utilized spectrophotometry and SED fitting from three sources. More recently, Southworth (2021) obtained a solution from a similar set of velocities and photometry from

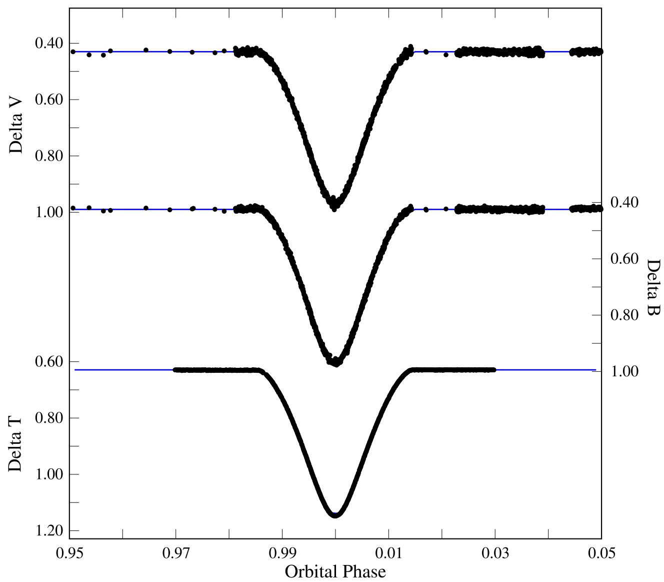

Figure 19. An expanded view of the primary eclipse for OT And.

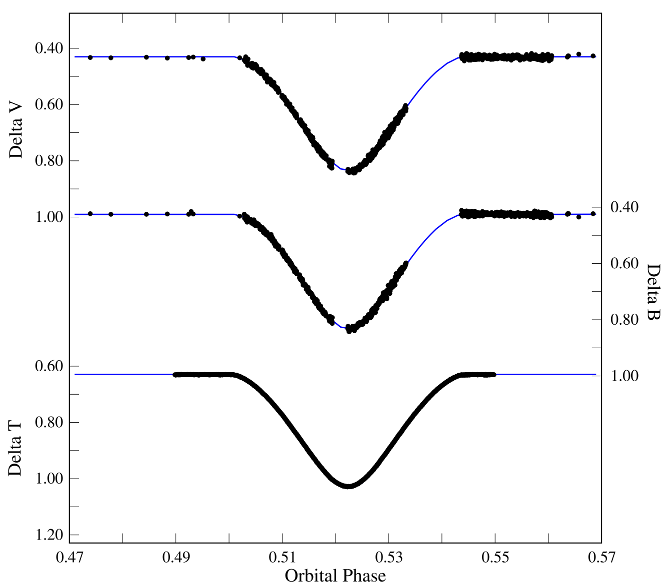

Figure 20. An expanded view of the secondary eclipse for OT And.

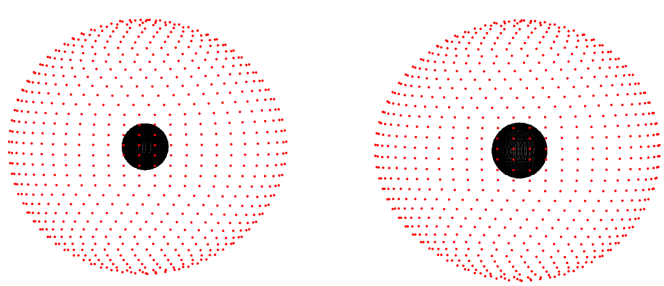

Figure 21. Image of OT And that is 0.08 in phase from periastron. The Roche lobes were computed by changing to the mode 6 option, and that solution is plotted in red.

the TESS space mission. Thus, we compare the derived properties of the three analyses. Table 22 lists our results for the masses, radii, temperatures, and other properties along with those of the other two analyses.

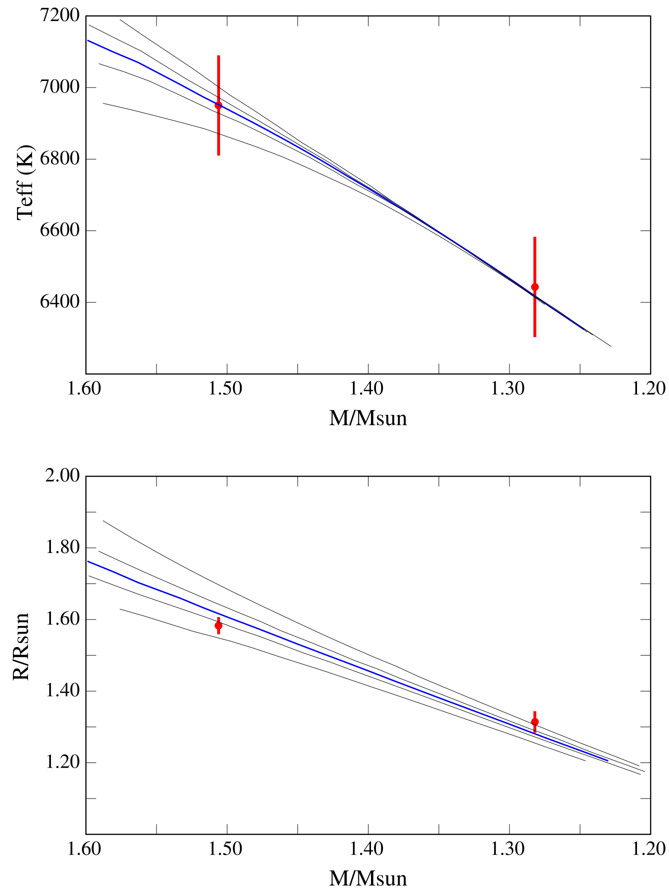

Figure 22. Mass–temperature and mass–radius diagrams comparing our values for the primary and secondary stars of HD 71636 with the MIST series model isochrones (Choi et al. 2016) for [Fe/H] = 0.12. Isochrones, increasing in age from bottom to top, between 0.6 and 1.2 Gyr in steps of 0.2 Gyr are indicated with solid black lines. The best-fit age of 0.9 Gyr is shown with a solid blue line.

Table 20
Model Radii of OT And

Parameter	Value
r_1 (pole)	0.0622 ± 0.0001
r_1 (point)	0.0622 ± 0.0001
r_1 (side)	0.0622 ± 0.0001
r_1 (back)	0.0622 ± 0.0001
r_2 (pole)	0.0520 ± 0.0001
r_2 (point)	0.0520 ± 0.0001
r_2 (side)	0.0520 ± 0.0001
r_2 (back)	0.0520 ± 0.0001

Table 21
Comparison of Fundamental Parameters of HD 71636

Parameter	Henry et al. (2006)	This Work
M_1 ($M_\odot$)	1.513 ± 0.009	1.506 ± 0.002
M_2 ($M_\odot$)	1.285 ± 0.007	1.282 ± 0.002
R_1 ($R_\odot$)	1.571 ± 0.009	1.583 ± 0.024
R_2 ($R_\odot$)	1.361 ± 0.008	1.314 ± 0.030
T_1 (K)	6950 ± 140	6950 ± 140
T_2 (K)	6440 ± 140	6443 ± 140
L_1 ($L_\odot$)	5.16 ± 0.43	5.26 ± 0.44
L_2 ($L_\odot$)	2.86 ± 0.25	2.68 ± 0.25

Table 22
Comparison of Fundamental Parameters of V1022 Cas

Parameter	Lester et al. (2019)	Southworth (2021)	This Work
M_1 ($M_\odot$)	1.626 ± 0.005	1.626 ± 0.001	1.626 ± 0.001
M_2 ($M_\odot$)	1.608 ± 0.005	1.609 ± 0.001	1.607 ± 0.001
R_1 ($R_\odot$)	2.65 ± 0.21	2.591 ± 0.026	2.570 ± 0.021
R_2 ($R_\odot$)	2.47 ± 0.23	2.472 ± 0.027	2.445 ± 0.022
i (deg)	97.1 ± 0.5	82.886 ± 0.006	82.92 ± 0.02
T_1 (K)	6450 ± 120	6450 ± 120	6350 ± 150
T_2 (K)	6590 ± 110	6590 ± 110	6420 ± 150
L_1 ($L_\odot$)	⋯	10.47 ± 0.82	9.67 ± 1.08
L_2 ($L_\odot$)	⋯	10.38 ± 0.72	9.15 ± 0.97

From their visual orbit, Lester et al. (2019) found an inclination of $97\overset{\circ}{.}1 \pm 0\overset{\circ}{.}5$, while the eclipse solution of Southworth (2021) produced an inclination of $82\overset{\circ}{.}886 \pm 0\overset{\circ}{.}006$, and our solution resulted in a value of $82\overset{\circ}{.}92 \pm 0\overset{\circ}{.}02$. Thus, all three inclinations differ from an edge-on orbit by $7\overset{\circ}{.}1$. With the use of similar radial-velocity data sets and the very similar determinations of the orbital inclination, the resulting masses from the three separate solutions are essentially identical (see Table 22).

The radii of the components derived by Lester et al. (2019) from spectrophotometry and SED fitting are in good agreement with the more precise results from eclipse solutions. A comparison of the radii derived from the TESS photometry used by Southworth (2021) with the values determined from our combined ground-based and TESS photometry shows excellent agreement. The temperatures that we adopt are 100 K and 170 K cooler for the primary and secondary, respectively, than those found by Lester et al. (2019) and adopted by Southworth (2021). As shown in Table 22, our resulting values of the components' luminosities with their uncertainties overlap those determined by Southworth (2021).

The good agreement of the basic properties from the astrometric-spectroscopic solution with those from the photometric-spectroscopic solutions lends support to the value of basic parameters that result from well-determined, spectroscopic-visual orbits plus spectrophotometry and spectrum fitting, with such analyses being particularly useful for noneclipsing systems.

Because the components of V1022 Cas are nearly identical, their properties provide little leverage in testing single-star evolutionary theory. The masses of the components of V1022 Cas have uncertainties of less than 0.1% each. Thus, we once again show mass–temperature and mass–radius diagrams (Figure 23). In them we compare our results (Table 16) with the MIST tracks (Choi et al. 2016). The solid lines are the model isochrones for ages, from left to right, that range from 1.7 to 2.1 Gyr in steps of 0.1 Gyr. The blue 1.9 Gyr age track is closest to the data points and indicates that the system age is about 1.87 Gyr. The system's components are well evolved and nearing the end of their main-sequence lifetimes.

The metallicity for our MIST track comparison is [Fe/H] = 0.08, which is the abundance that provides the best match to the effective temperatures. From the various fits, we estimate an abundance uncertainty of ± 0.02. From an abundance analysis of V1022 Cas, when the lines of the components were blended, Balachandran (1990) obtained an [Fe/H] value of -0.01 ± 0.17, so a solar abundance. Given the nearly identical basic parameters of the components, it is reasonable to assume this abundance for both stars. Lester et al. (2019) and Southworth (2021) adopted slightly hotter temperatures for the components and, as a result of their comparisons with various evolutionary models, concluded that the stars have solar metallicity. Given its uncertainty, the abundance value of Balachandran (1990) encompasses both a solar abundance value and our slightly metal-rich result.

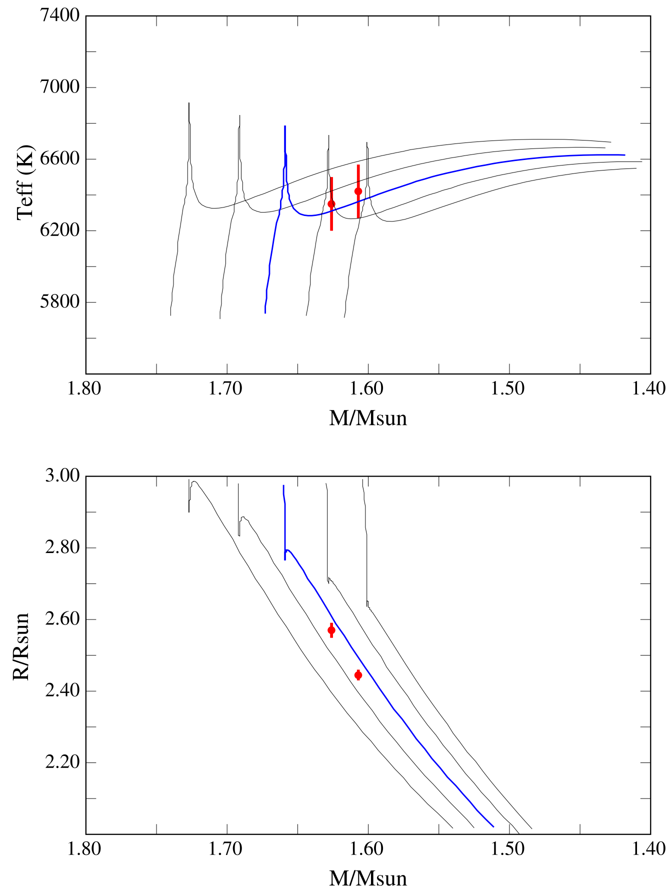

Figure 23. Mass–temperature and mass–radius diagrams comparing our values for the primary and secondary stars of V1022 Cas with the MIST series model isochrones (Choi et al. 2016) for [Fe/H] = 0.08. Isochrones, increasing in age from left to right, range in age from 1.7 to 2.1 Gyr in steps of 0.1 Gyr and are indicated with solid lines. The components are closest to the solid blue line, which has an age of 1.9 Gyr, so we estimate the age of the system as 1.87 Gyr.

Our WD analysis of the nearly identical components of V1022 Cas, as well as that of Southworth (2021), produces uncertainties of $\leqslant$1% for the masses and the radii. Thus the V1022 Cas system joins the list of over 90 detached eclipsing binaries with masses and radii determined to better than 3% that was compiled by Torres et al. (2010). Given previous spectral classifications of its composite spectrum and the very similar effective temperatures and radii of the components, we adopt F6 V spectral types for both components.

Being an eccentric system, V1022 Cas has apsidal motion consisting of both a Newtonian component and a relativistic component (e.g., Giménez 1985). A rather similar system is BF Dra, a mid-F-type eclipsing binary having an orbit with a period of 11.21 days and eccentricity of 0.39. From about 80 yr of eclipse timings for BF Dra, Lacy et al. (2012) determined a total apsidal motion of $0\overset{\circ}{.}00049$ cycle^{-1} or $1\overset{\circ}{.}60$ century^{-1}. More recently, from additional eclipse timings Claret et al. (2021) obtained a significantly smaller total apsidal rate of

$0\overset{\circ}{.}00037$ cycle^{-1} or $1\overset{\circ}{.}21$ century^{-1}. From Equation (3) of Giménez (1985), the relativistic apsidal rate of BF Dra is $0\overset{\circ}{.}00025$ cycle^{-1} or $0\overset{\circ}{.}81$ century^{-1}. Subtracting this value from the two different measurements of the total rate, the difference between the two Newtonian values indicates that there is significant uncertainty in the Newtonian rate, but in both cases the relativistic component is greater than that of the Newtonian.

For V1022 Cas we determine a relativistic apsidal rate of $0\overset{\circ}{.}00025$ cycle^{-1}, the same as for BF Dra. However, V1022 Cas has a period of 12.16 days, which is 8.5% longer. This results in a relativistic apsidal motion of $0\overset{\circ}{.}75$ century^{-1}, a decrease of 7.4% compared with that of BF Dra.

Giménez (1985) has pointed out that the period dependence of the two components of apsidal motion is quite different. The Newtonian apsidal motion is proportional to $P^{-10/3}$ while the relativistic apsidal motion is proportional to $P^{-2/3}$, so this large difference causes the Newtonian value to decrease much faster than the relativistic value.

Recently, for V1022 Cas Claret et al. (2021) have determined a total apsidal rate of $0\overset{\circ}{.}00032$ cycle^{-1}. Subtracting the relativistic rate results in a smaller Newtonian term of just $0\overset{\circ}{.}00007$ cycle^{-1} or $0\overset{\circ}{.}21$ century^{-1}.

6.3. *OT And*

From our WD analysis, the masses and radii of OT And have uncertainties of less than 1%. Thus OT And also joins the list of detached eclipsing binaries with well-determined basic parameters that was compiled by Torres et al. (2010).

Once again, we show mass–temperature and mass–radius diagrams (Figure 24). In them we compare our results (Table 19) with the MIST tracks (Choi et al. 2016). The solid black lines are the model isochrones for ages, from left to right, of 0.60–0.75 Gyr in steps of 0.05 Gyr. The solid blue line is a good fit to the data points and indicates that the system age is 0.675 Gyr. The metallicity for this comparison is [Fe/H] = 0.10, which is the abundance that provides the best match to the effective temperatures. From the various fits, we estimate an abundance uncertainty of ±0.03. Note that the primary is farther along the main sequence and therefore cooler than the secondary.

Like V1022 Cas, OT And is an eccentric system. From Equation (3) of Giménez (1985), its relativistic apsidal motion is $0\overset{\circ}{.}00020$ cycle^{-1} or just $0\overset{\circ}{.}36$ century^{-1}. Its period of 20.853 days is 1.7 times longer than that of V1022 Cas. As noted previously, the Newtonian apsidal motion has a much greater period dependence than the relativistic component, so the latter is certainly the dominant source of apsidal motion for OT And.

7. Summary

Our differential *BV* photometry, open access TESS data, and our radial-velocity measurements for HD 71636, V1022 Cas, and OT And have been analyzed with the WD software. For HD 71636 we obtain an improved solution that now produces consistent ages for the components. The masses and radii from our combined ground-based and TESS WD solution of V1022 Cas are in good agreement with the results of the TESS space mission photometry (Southworth 2021) and the combined spectroscopic and interferometric results of Lester et al. (2019). Our slightly lower effective temperatures for its

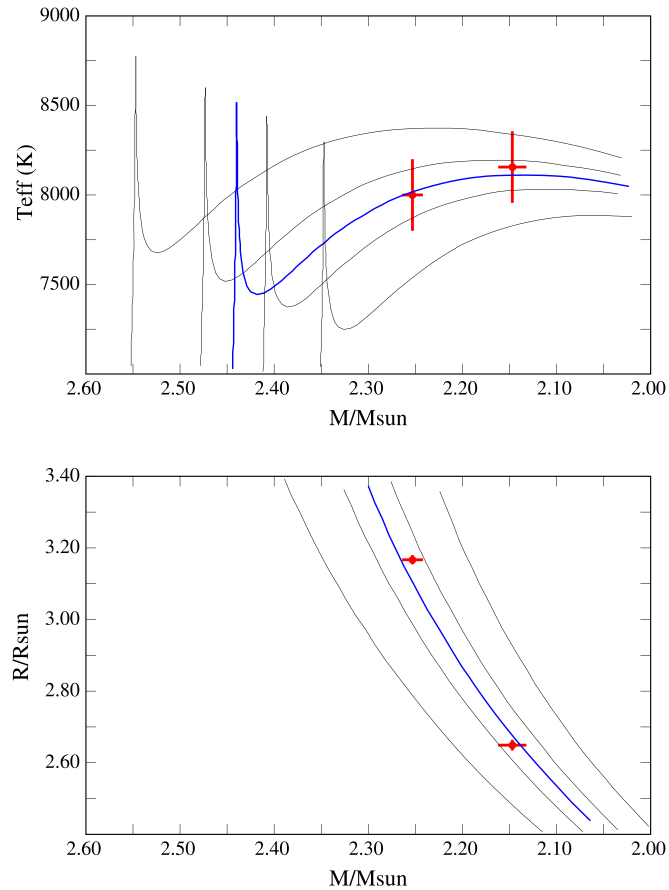

Figure 24. Mass–temperature and mass–radius diagrams comparing our values for the primary and secondary stars of OT And with the MIST series model isochrones (Choi et al. 2016) for [Fe/H] = 0.10. Isochrones, increasing in age from left to right, range from 0.60 to 0.75 Gyr in steps of 0.05 Gyr and are indicated with solid black lines. The best-fit age of 0.675 Gyr is indicated by a solid blue line.

components result in best-fit theoretical models to the observed properties that, unlike previous solutions, need no extinction but result in a slightly metal-rich composition. For OT And the analysis of our radial velocities and photometry produces, for the first time, the masses and radii of the components and their evolutionary status. For all three systems, the separate analyses of the ground-based photometry and the more precise TESS photometry produce very similar results, with the TESS data generally having results with somewhat reduced uncertainties. Both V1022 Cas and OT And have eccentric orbits, but with relatively long orbital periods of 12.156 days and 20.853 days, respectively, the total apsidal motion in both systems is less than $1\overset{\circ}{.}5$ century^{-1}. The characteristics of the stars have high quality and precision, and they should be very useful in future studies of stellar parameters and evolution.

We greatly appreciate the referee's time and comments that significantly improved the usefulness of this paper. We thank Walter Van Hamme (Florida International University) for discussions about the WD program's various aspects and for assistance with error bars. Astronomy at Tennessee State University is supported by the state of Tennessee through its Centers of Excellence program. Our research made use of the SIMBAD database, operated by CDS in Strasbourg, France. This work also made use of data from the European Space Agency (ESA) mission Gaia (https://www.cosmos.esa.int/gaia), processed by the Gaia Data Processing and Analysis Consortium (DPAC, https://www.cosmos.esa.int/web/gaia/dpac/consortium). Funding for the DPAC has been provided by national institutions, in particular the institutions participating in the Gaia Multilateral Agreement. This paper includes data collected by the TESS mission. Funding for the TESS mission is provided by the NASA's Science Mission Directorate.

Facility: Fairborn Observatory.

ORCID iDs

Francis C. Fekel https://orcid.org/0000-0002-9413-3896
Gregory W. Henry https://orcid.org/0000-0003-4155-8513
James R. Sowell https://orcid.org/0000-0003-3480-0957
Ethan R. Partington https://orcid.org/0000-0003-1183-1574

References

Abt, H. A. 2009, ApJS, 180, 117
Abt, H. A., & Bidelman, W. 1969, ApJ, 158, 1091
Agerer, F., & Hübscher, J. 2001, IBVS, 5016, 1
Agerer, F., & Hübscher, J. 2003, IBVS, 5484, 1
Balachandran, S. 1990, ApJ, 354, 310
Barker, E. S., Evans, D. S., & Laing, J. D. 1967, RGOB, 130, 355
Batten, A. H., Fletcher, J. M., & MacCarthey, D. G. 1989, PDAO, 17, 1
Casagrande, L., Schönrich, R., Asplund, M., et al. 2011, A&A, 530, A138
Choi, J., Dotter, A., Conroy, C., et al. 2016, ApJ, 823, 102
Claret, A., Giménez, A., Baroch, D., et al. 2021, A&A, 654, 17
Clausen, J. V., Frandsen, S., Bruntt, H., et al. 2010, A&A, 516, A42
Cowley, A. 1976, PASP, 88, 95
Crawford, D. L. 1975b, AJ, 80, 955
Crawford, R. C. 1975a, BAAS, 7, 294
Crawford, R. C., Ingvarsson, S. I., Boyd, L. J., et al. 1984, IBVS, 2624, 1
Eaton, J. A., Henry, G. W., & Fekel, F. C. 2003, in The Future of Small Telescopes in the New Millennium, Volume II—The Telescopes We Use, ed. T. D. Oswalt (Dordrecht: Kluwer), 189
Eaton, J. A., & Williamson, M. H. 2004, SPIE, 5496, 710
Eaton, J. A., & Williamson, M. H. 2007, PASP, 119, 886
Eker, Z., Bakis, V., Bilir, S., et al. 2018, MNRAS, 479, 5491
ESA 1997, ESA SP-1200, The Hipparcos and Tycho Catalogues (ESA: Noordwijk)
Fekel, F. C., & Griffin, R. F. 2011, Obs, 131, 283
Fekel, F. C., Rajabi, S., Muterspaugh, M. W., & Williamson, M. H. 2013, AJ, 145, 111
Fekel, F. C., Tomkin, J., & Williamson, M. H. 2009, AJ, 137, 3900
Fekel, F. C., Tomkin, J., & Williamson, M. H. 2010, AJ, 139, 1579
Flower, P. J. 1996, ApJ, 469, 355
Gaia Collaboration, Brown, A. G. A., Vallenari, A., et al. 2021, A&A, 649, A1
Giménez, A. 1985, ApJ, 297, 405
Gray, D. F. 1992, The Observations and Analysis of Stellar Photospheres (Cambridge: Cambridge Univ. Press), 431
Green, G. M., Schlafly, E. F., Zucker, C., Speagle, J. S., & Finkbeiner, D. P. 2019, ApJ, 887, 93
Hall, D. S. 1983, IAPPP Communication, 13, 6
Harper, W. E. 1923, PDAO, 2, 263
Henry, G. W. 1995a, in ASP Conf. Ser. 79, Robotic Telescopes: Current Capabilities, Present Developments, and Future Prospects for Automated Astronomy, ed. J. A. Henry & G. W. Eaton (San Francisco: ASP), 37
Henry, G. W. 1995b, in ASP Conf. Ser. 79, Robotic Telescopes: Current Capabilities, Present Developments, and Future Prospects for Automated Astronomy, ed. G. W. Henry & J. A. Eaton (San Francisco: ASP), 44
Henry, G. W., Fekel, F. C., & Henry, S. M. 2005, AJ, 129, 2815
Henry, G. W., Fekel, F. C., Sowell, J. R., & Gearhart, J. S. 2006, AJ, 132, 2489
Høg, E., Fabricius, C., Makarov, V. V., et al. 2000, A&A, 355, L27
Husar, D. 2005, OEJV, 10, 1
Kazarovets, E. V., Samus, N. N., Durlevich, O. V., Kireeva, N. N., & Pastukhova, E. N. 2008, IBVS, 5863, 1
Kholopov, P. N., Samus, N. N., Kazarovets, E. V., & Kireeva, N. N. 1987, IBVS, 3058, 1
Lacy, C. H. S., Torres, G., Fekel, F. C., Sabby, J. A., & Claret, A. 2012, AJ, 143, 129
Lester, K. V., Gies, D. R., Schaefer, G. H., et al. 2019, AJ, 157, 140
Lucy, L. B. 1967, ZA, 65, 89
Masana, E., Jordi, C., & Ribas, I. 2006, A&A, 450, 735
Maxted, P. F. L., Gaulme, P., Graczyk, D., et al. 2020, MNRAS, 498, 332
Nordström, B., Mayor, M., Andersen, J., et al. 2004, A&A, 418, 989
Otero, S. 2006, IBVS, 5699, 1
Paunzen, E. 2015, A&A, 580, 23
Paxton, B., Bildsten, L., Dotter, A., et al. 2011, ApJS, 192, 3
Paxton, B., Cantiello, M., Arras, P., et al. 2013, ApJS, 208, 4
Paxton, B., Marchant, P., Schwab, J., et al. 2015, ApJS, 220, 15
Plaskett, J. S., Harper, W. E., Young, R. K., & Plaskett, H. H. 1920, PDAO, 1, 163
Prsa, A., Harmanec, P., Torres, G., et al. 2016, AJ, 152, 41
Ricker, G. R., Winn, J. N., Vanderspek, R., et al. 2015, JATIS, 1, 014003
Sandberg Lacy, C. H., & Fekel, F. C. 2011, AJ, 142, 185
Scarfe, C. D. 2010, Obs, 130, 214
Southworth, J. 2021, Obs, 141, 52
Southworth, J. 2022, Obs, 140, 247
Torres, G., Andersen, J., & Gimenez, A. 2010, A&ARv, 18, 67
Tremko, J., & Bakos, G. A. 1978, JRASC, 72, 263
Van Hamme, W. 1993, AJ, 106, 2096
Van Hamme, W., & Wilson, R. E. 2007, ApJ, 661, 1129
Wilson, R. E. 1979, ApJ, 234, 1054
Wilson, R. E. 1990, ApJ, 356, 613
Wilson, R. E. 2012a, JASS, 29, 115
Wilson, R. E. 2012b, AJ, 144, 73
Wilson, R. E., & Devinney, E. J. 1971, ApJ, 166, 605
Wilson, R. E., & Van Hamme, W. 2014, ApJ, 780, 151
Wilson, R. E., Van Hamme, W., & Terrell, D. 2010, ApJ, 723, 1469
Wolfe, R. H., Horak, H. G., & Storer, N. W. 1967, in Modern Astrophysics, ed. M. Hack (New York: Gordon & Breach), 251